The transcriptional response of cortical neurons to concussion reveals divergent fates after injury

Mor R. Alkaslasi[1,2], Eliza Y. H. Lloyd[1], Austin S. Gable[1], Hanna Silberberg[1], Hector E. Yarur[3], Valerie S. Tsai[3], Hugo A. Tejeda[3], Claire E. Le Pichon*[,1]

[1]Unit on the Development of Neurodegeneration, *Eunice Kennedy Shriver* National Institute of Child Health and Human Development, National Institutes of Health, Bethesda, MD, USA

[2]Department of Neuroscience, Brown University, Providence, RI, USA

[3]Unit on Neuromodulation and Synaptic Integration, National Institute of Mental Health, National Institutes of Health, Bethesda, MD, USA.

* Correspondence: claire.lepichon@nih.gov

Abstract

Traumatic brain injury (TBI) is a risk factor for neurodegeneration, however little is known about how different neuron types respond to this kind of injury. In this study, we follow neuronal populations over several months after a single mild TBI (mTBI) to assess long ranging consequences of injury at the level of single, transcriptionally defined neuronal classes. We find that the stress responsive Activating Transcription Factor 3 (ATF3) defines a population of cortical neurons after mTBI. We show that neurons that activate ATF3 upregulate stress-related genes while repressing many genes, including commonly used markers for these cell types. Using an inducible reporter linked to ATF3, we genetically mark damaged cells to track them over time. Notably, we find that a population in layer V undergoes cell death acutely after injury, while another in layer II/III survives long term and retains the ability to fire action potentials. To investigate the mechanism controlling layer V neuron death, we genetically silenced candidate stress response pathways. We found that the axon injury responsive kinase MAP3K12, also known as dual leucine zipper kinase (DLK), is required for the layer V neuron death. This work provides a rationale for targeting the DLK signaling pathway as a therapeutic intervention for traumatic brain injury. Beyond this, our novel approach to track neurons after a mild, subclinical injury can inform our understanding of neuronal susceptibility to repeated impacts.

Introduction

Close to half the population is expected to experience a mild traumatic brain injury (mTBI) at some point in their life[1]. A common form of mTBI is concussion, a brain injury caused by mechanical force and resulting in temporary neurological dysfunction. Although most people seemingly recover, for some the impact can lead to long term damage. There is increasing evidence that repeated mTBI can cause chronic traumatic encephalopathy (CTE)[2] and is a potential risk factor for other neurodegenerative disorders[3–5]. The primary insult of mTBI triggers a cascade of damage termed 'secondary injury' that involves multiple brain cell types and unfolds during the days and weeks following the impact[1]. Even if symptoms during this time can be relatively mild, it is during this chronic phase that neurons are thought to become more vulnerable to repeated injuries. Despite this, the typical treatment for mild TBI is limited to pain management and rest. It is therefore likely that neuroprotective treatments would be beneficial to stave off risk of permanent damage.

To develop effective treatments, we must first better understand the pathways initiated in particular neurons. Many studies to date have lacked the resolution to discern cell type-specific responses[6–8]. More recent work has examined the effect of injury on particular neuron types[9,10]. We reasoned that a detailed look at a model of single mild TBI would provide important insight into the nature and extent of neuronal injury immediately following a concussion. We previously generated a mouse line to track neurons that are transcriptionally responsive to peripheral nerve injury[11] and wondered if it could be used to investigate mTBI. Peripheral nerve injuries cause a transcriptional response in sensory neurons that is regulated by *Atf3* (activating transcription factor 3) and is essential for functional recovery[11,12]. In sensory neurons, *Atf3* is responsible for upregulating select regeneration-associated genes while repressing many other genes to promote recovery. We wondered whether a similar transcriptional response might occur in the brain after mTBI. If so, how would these neurons compare to peripheral sensory neurons in their ability to exhibit plasticity and recover?

Using genetic reporter mice, single nucleus RNA-sequencing, and slice electrophysiology, we performed a detailed characterization of the neurons that transcriptionally activate *Atf3* after mTBI. We demonstrate that several subtypes of cortical neurons engage the *Atf3* response, but that these undergo divergent fates (death vs survival) that are linked to their identities. We probe the role of multiple candidate pathways for their contribution to cortical neuron death after mTBI and find that dual leucine zipper kinase (DLK), an upstream regulator of *Atf3*, drives neuron death in layer V, highlighting it as a potential therapeutic target for mTBI. These results underscore a differential vulnerability of cortical neurons to mTBI and emphasize the importance of studying injury-induced pathology at the level of individual neuronal subtypes.

Results

Characterizing neurodegeneration in a closed skull model of mild TBI

To study mild TBI, we characterized a unilateral closed-skull injury model[13] that provides a clinically relevant view of concussion injury and allowed us to accurately dissect the resulting pathological cascade. We used a controlled cortical impact injury wherein an impact was delivered directly to the surface of the skull at a specified depth and velocity. The impact was provided by a 3 mm diameter tip positioned over the mouse's left sensorimotor cortex (Fig. 1a). Following this injury, mice presented with no overt symptomology and no tissue loss, but do exhibit reproducible cortical astrogliosis in an area approximately 2 mm in diameter and confined to the ipsilateral cortex (Fig. 1b). This model resulted in a loss of righting reflex concordant with mild TBI (righting time < 15 minutes[14,15], Fig. 1c), as well as a small yet consistent increase in the serum biomarker of neuron degeneration, Neurofilament Light[16] (NfL, average 3-fold higher than baseline between 1-14 dpi, Fig. 1d).

We started by examining pathology in the Thy1-YFP-H mouse, which sparsely expresses a fluorescent protein in layer V cortical neurons, highlighting their morphology[17,18]. We histologically confirmed cortical neurodegeneration in these mice (Fig. 1e). At 7 days post injury (dpi), we observed hallmarks of degenerating dendrites, cell bodies, and axons specifically in the ipsilateral cortex but not the side contralateral to injury (Fig. 1e-k, Supplementary Fig. 1a). Cortical dendrite fragmentation in the region above layer V was quantified using a degeneration index calculation[19] and revealed significant degeneration of YFP+ dendrites[20] only in the ipsilateral cortex when compared to the contralateral side or the ipsilateral cortex of sham injury controls (Fig. 1f,i). Below layer V there was a significant increase in YFP-positive structures that did not correspond to cell bodies but rather to pathological enlargements of axons (area = 10-250 μm^2, mean = 20 μm^2, Fig. 1h,j). Some of these axonal swellings were of comparable size to cell bodies (none contained DAPI-positive nuclei, Supplementary Fig. 1b). The swellings likely correspond to disruption in axon transport leading to organellar and protein accumulations, also called diffuse axonal injury[9,21–23]. We also observed beading of axons (fragments < 10 μm^2) representing axon degeneration. We found that both axon beading and swelling were increased only in the ipsilateral cortex at 7 dpi (Fig. 1h,j).

Because the Thy1 reporter is stochastically expressed, and because we had specifically observed inflammatory, dendritic, and axonal pathology only on the side ipsilateral to injury, to quantify any potential cell loss, we compared the number of YFP+ neurons in the cortex ipsilateral to the injury, and normalized them to the contralateral cortex of each section. We measured a 15.3% ± 1.8 loss of cell bodies at 7 dpi, and 26.3% ± 7.9 loss at 14 dpi (Fig. 1e,k). Thus, we find that a single unilateral closed head impact over the sensorimotor cortex reproducibly leads to progressive degeneration of layer V projection neurons ipsilateral to the injury and across neuronal compartments.

mTBI produces an Atf3 response in a subset of cortical neurons

Transcription factors play major roles in neuronal responses to injury, and their activation can determine whether a neuron degenerates or regenerates. The transcription factor ATF3, in particular, is a master regulator of the transcriptional response to neuronal injury, and is responsible for driving a transcriptional shift toward an injured cell state[11,12]. We looked for ATF3 expression in brains following mTBI and observed that at 7 dpi, ATF3 immunolabeling localized specifically to the injured side of the cortex (Fig. 2a). We found 10% ± 2.3 of YFP-expressing neurons expressing ATF3 at this timepoint[24] (Fig. 2b). Some ATF3-positive cells were also present in layer II/III (Fig 2a).

Our initial attempts to identify the ATF3-positive neurons in layer V using markers of projection neurons such as CTIP2[25] were unsuccessful. We observed no double labeled cells upon staining for ATF3 and CTIP2 (Fig. 2d-f). We reasoned that ATF3 might be repressing marker genes in the cortex after TBI as has been observed in peripheral sensory neurons after axon injury[11,12]. We therefore performed single nucleus RNA sequencing of these neurons to obtain a more comprehensive picture of their repertoire of RNA expression.

Transcriptional profiling of cells that activate Atf3 in the injured cortex

We employed targeted snRNAseq of *Atf3*-expressing neurons using an inducible Atf3-IRES-CreER mouse line[12] crossed to the INTACT nuclear envelope protein reporter[26]. Tamoxifen was administered at 4 and 5 dpi to induce expression of the nuclear GFP reporter and tissue was collected at 7 dpi, enabling the isolation of all cells expressing *Atf3* during this acute phase (Fig. 2c).

We sequenced 8,171 GFP+ nuclei and found a significant number of microglia (4067, 49.8%), excitatory (2792, 34.2%) and inhibitory (701, 8.6%) neurons, and small populations of astrocytes (115, 1.4%), oligodendrocytes (75, 0.9%), and other cells (421, 5.1%) (Supplementary Fig. 2a-e). In this study we focus on the role of ATF3 as an injury marker in neurons, but we note its role in microglial function as an interesting avenue for future investigation[27,28].

Specific subtypes of excitatory and inhibitory cortical neuron subtypes activate Atf3-associated injury pathways

We mapped the neuronal nuclei from this experiment onto a highly annotated mouse motor cortex reference atlas[29] to assign cellular subtypes based on the nuclear transcriptome. Of the 2,975 neuronal nuclei sequenced using the Atf3-CreER approach, we identified excitatory neurons across cortical layers, parvalbumin (Pvalb) and somatostatin (Sst) interneurons, and small numbers of Lamp5, Vip, and Sncg interneurons (Fig. 2d,f, Supplementary Fig. 2a,b, Supplementary Table 1). Using multiplex *in situ* hybridization with markers from the data, we validated the presence of Gfp+ excitatory and inhibitory neurons (Supplementary Fig. 3a-c).

Interestingly, all interneuron subtypes expressed the inhibitory neuron marker *Gad2*, but lacked their subtype markers, including *Pvalb* or *Sst* (Fig. 2f). Similarly, neurons assigned to excitatory cortical layer identities lacked the typical expression of *Slc17a7* (VGLUT1), but expressed some layer-specific markers, such as *Cux2*, *Rorb*, and *Foxp2* (Fig. 2f). Thus, in the cortex - similar to the peripheral sensory nervous system[11,12] - Atf3 expression leads to the downregulation of multiple marker genes.

In our experiment, we captured neurons that had expressed *Atf3* at 4 and 5 dpi, and sequenced them at 7 dpi. Some of these still expressed *Atf3*, but many only had low or undetectable *Atf3* expression (Fig. 2g, Supplementary Fig. 3a). In contrast, the damage-induced neuronal endopeptidase *Ecel1*, whose expression is directly downstream of *Atf3*[30], was highly expressed in both excitatory and inhibitory neurons (Fig. 2g, Supplementary Fig. 3a). We investigated the expression of a panel of injury-induced genes across neuronal subtypes and discovered that not all neuron subtypes that activated *Atf3* underwent the same subsequent transcriptional programs (Fig. 2g). For example, pro-apoptotic and endoplasmic reticulum (ER) stress genes such as *Ddit3*[31] were most highly expressed in layer V neurons and low in layer II/III (validated by in situ hybridization, Supplementary Fig. 3d), while *Atf3* and axon growth genes were most highly expressed in Pvalb and other interneuron subtypes. Thus although many neurons upregulate Atf3, their overall transcriptional changes differ depending on cell type. Our data thus highlight heterogeneous transcriptional programs and fates among the Atf3-captured neurons.

Genetic labeling of Atf3-expressing neurons highlights layer-specific vulnerability

To visualize and map the neurons that express *Atf3* after mTBI, we generated a neuron-specific *Atf3* reporter mouse (Atf3-GFP) in which GFP is permanently expressed only in neurons once *Atf3* is upregulated. In control mice, sparse GFP labeling is observed in the cortex and in some hippocampal neurons, likely due to developmental Atf3 expression (Supplementary Fig. 4a). We assessed the extent of Atf3-GFP labeling in the cortex and in other brain regions, observing injury-induced GFP primarily on the ipsilateral side of the cortex, as well as in the ipsilateral anterior thalamic nuclei (Supplementary Fig. 4b). The anterior thalamic neurons project into the cortex around the site of injury, and thus their axons may be damaged in this injury model[32,33].

Because this Cre-dependent system results in permanent labeling of neurons in which *Atf3* is induced, we concluded that loss of GFP-expressing neurons together with signs of neurodegenerative pathology would indicate cell death. Longitudinal quantification up to 70 dpi of GFP-expressing neurons in the ipsilateral cortex revealed that a prominent group of layer V cortical neurons expressed Atf3-dependent GFP between 5 and 10 dpi and subsequently disappeared by 14 dpi, while a population of layer II/III neurons persisted at 70 dpi (Fig. 3a,b). The loss of layer V Atf3-GFP neurons by 14 dpi echoes the layer V neuron loss observed in the Thy1-YFP mouse (Fig. 1e,f). Parallel quantification of ATF3 protein revealed a comparative delay in GFP expression and extensive activation of ATF3 in non-neuronal cells, which was consistent with our snRNAseq data (Supplementary Fig. 5a). Interestingly, amplification of GFP signal with

immunolabeling revealed that some layer II/III neurons initially exhibit lower expression of GFP (Fig. 3b).

Layer V Atf3-expressing neurons undergo cell death and are phagocytosed following mTBI

Atf3 activation promotes axon regeneration in peripheral injuries, but here we found its expression in neurons that are unlikely to regenerate. Because GFP+ neurons at 7 dpi were present only on the ipsilateral side of the cortex and primarily in layer V (Supplementary Fig. 5c), we were able to use the stereotyped projection patterns of layer V neurons to inspect the dendrites and axons of these neurons. Similarly to the Thy1-YFP+ layer V neurons (Fig 1e-k), we discovered that the GFP+ dendrites were severely fragmented, indicating dendrite degeneration, while GFP+ axons exhibited axonal swellings typical of diffuse axonal injury (Supplementary Fig. 5a). Morphologically unhealthy neurons that exhibited cell body vacuolization and loss of nuclear DAPI signal were also observed in layer V (Supplementary Fig. 5a, d).

Neuron death in layer V was confirmed by examining the expression of several types of apoptotic markers in Atf3-GFP tissue. The pro-apoptotic gene *Ddit3*[31] was significantly increased in GFP+ neurons compared to GFP-negative neurons either ipsilateral or contralateral to injury. In GFP+ neurons with high *Ddit3* expression, we observed high DAPI intensity reflecting chromatin condensation during apoptosis[34] (Supplementary Fig. 5d,e). These apoptotic cells had lower GFP expression and appeared morphologically misshapen (shriveled/deformed, Supplementary Fig. 5c). Additionally, the DNA damage marker phospho-H2AX, which is phosphorylated during apoptosis[35], was elevated in GFP+ neurons at 10 dpi but not in GFP- neurons in the ipsilateral or contralateral cortex (Supplementary Fig. 5f,g). The specificity of phospho-H2AX upregulation to GFP+ neurons and not their GFP- neighbors highlights that this mechanism of cell death is specific to neurons undergoing *Atf3*-associated injury responses at this timepoint. Thus, we conclude that layer V neurons that activate *Atf3* undergo apoptosis in the weeks following injury.

Related to this neuron death, we found that microglia exhibited increased phagocytic activity in the ipsilateral cortex and engulfed debris from dead GFP+ neurons. A significant proportion of CD68+ microglial lysosomes contained GFP+ debris (10% ± 4.2 of at 7 dpi) which increased by 14 dpi (15% ± 3.5), and coincided with the maximal loss of layer V neurons (Supplementary Fig. 5h,i). Microgliosis occurred specifically in the ipsilateral cortex where it peaked around 10 dpi and returned to baseline by 42 dpi (Supplementary Fig. 6a,b). Astrogliosis occurred in a delayed yet prolonged peak of GFAP expression which remained elevated at 70 dpi (Supplementary Fig. 6a,c).

These findings demonstrate mTBI leads to activation of *Atf3*-associated pathways in layer V cortical neurons, to their degeneration and death within two weeks after injury, and to cortical glial responses.

Layer II/III Atf3-expressing neurons survive and remain electrophysiologically active

The analysis of Atf3-GFP neurons across cortical layers over time (Fig. 3a) revealed the loss of most GFP-positive layer V neurons, and highlighted those in layer II/III as the main surviving GFP-positive population at 70 dpi. To evaluate whether this resulted from long-term survival of *Atf3*-marked neurons, we used the inducible *Atf3* reporter line. By injecting tamoxifen at 4 and 5 days post injury, we could permanently label cells expressing *Atf3* at this time point and evaluate their localization over time (Fig. 3c). While most labeled neurons at 7 dpi were located in layer V, those remaining at 21 dpi were primarily found in layer II/III. These layer II/III *Atf3*-marked neurons persisted until at least 42 dpi (Supplementary Fig. 7a), and likely represent a resilient population of neurons that activate this stress response pathway soon after injury and survive. Additionally, layer II/III neurons at 21 dpi appeared morphologically healthy, unlike the degenerative profiles observed in some layer V neurons at 7 dpi (Supplementary Fig. 7b,c).

Next, we determined whether Atf3-GFP neurons displayed injury-induced alterations in excitability and basic membrane properties. We hypothesized the neurons would traverse a cellular state with altered electrophysiological properties reflecting the Atf3-response, and that this would differ between neurons from layer V versus layer II/III. We performed whole-cell patch clamp recordings of excitatory neurons from the neuron-specific Atf3-GFP mice at an acute (5-7 dpi) and late (21 dpi) timepoint. At the acute timepoint, layer II/III neurons expressed low levels of endogenous GFP and were thus too sparse and poorly defined to record from (Fig. 3b). Therefore, at this timepoint, we only recorded from GFP+ neurons in Layer V.

Layer V neurons at the acute stage were sufficiently healthy to record from, therefore not yet undergoing apoptosis, but they had clear alterations in electrophysiological properties compared to GFP-negative control neurons in the ipsilateral or contralateral cortex. They exhibited reduced intrinsic excitability: they were unable to sustain repetitive regular firing (Fig. 4a,b), had a higher rheobase (the minimal current required to initiate an action potential), and a significant decrease in the maximum number of spikes produced (Fig. 4c,d). They were also more depolarized (-54 mV vs -68 mV in controls, Fig. 4e). However, their lowered excitability did not stem from alterations in passive membrane properties since these were no different from controls (input resistance, Supplementary Fig. 7f, and capacitance, which reflects cell size and/or arborization complexity, Fig 4f).

GFP-negative neurons in the ipsilateral cortex were indistinguishable from contralateral uninjured neurons by nearly all measures, suggesting the decline in intrinsic excitability observed in GFP+ layer V neurons is a specific consequence in Atf3-positive neurons. Consistent with this, in our snRNAseq profiling of Atf3-captured neurons, we noted a pattern of downregulation of ion channels involved in action potential firing and maintenance of membrane potential (Fig. 4g). We confirmed the downregulation of *Scn1a* and *Kcnq5* in GFP+ layer V neurons in the tissue (Fig. 4h). The downregulation of these genes provides an explanation for the changes in excitability we observed in the Atf3-marked neurons.

At the later time point, 21 dpi, Atf3-GFP layer II/III neurons were able to maintain sustained firing, similar to GFP-negative controls (Fig. 4i, j, l). However, they exhibited increased tonic firing (Supplementary Fig. 7h), decreased rheobase threshold (Fig. 4k), increased input resistance (Supplementary Fig. 7j), and depolarized membrane potential (-53 mV vs –66 mV in controls, Fig. 4m) - all measures that reflect increased excitability. GFP+ neurons also exhibited a reduced capacitance, suggesting that they might be more compact and/or less complex than GFP- controls (Fig. 4n). Interestingly, amplified hyperpolarization-activated (Ih) current, an inward current that is important in regulating action potential firing frequency, may contribute to enhanced tonic firing in GFP+ neurons in layer II/III[36,37] (Supplementary Fig. 7k, i). Together, these findings suggest that surviving layer II/III Atf3-GFP neurons adapt passive membrane properties to maintain sustained firing.

Layer II/III neurons undergo axon initial segment reorganization following mTBI

Because we found that GFP+ neurons in layer II/III survive but are hyperexcitable, we wondered what the consequences would be on their output. We therefore examined whether their axon initial segment (AIS) underwent alterations. The AIS is a specialized structure at the base of the axon that is essential for generating action potentials[38,39]. Other neuron types have been reported to transiently lose their AIS during regeneration[40–42]. Immunolabeling for Ankyrin-G, a master scaffolding protein of the AIS, suggested that the AIS in layer II/III neurons was lost at 7 dpi but regained by 14 dpi (Supplementary Fig. 8a-c). This transient loss of AIS markers was confirmed with staining for another AIS protein, β4-spectrin (Supplementary Fig. 8d). The hyperexcitability observed at 21 dpi in layer II/III neurons may be linked to a reorganization of the AIS after mTBI. By contrast, layer V neurons did not lose their AIS (Supplementary Fig. 8a-d). Previous studies of closed skull TBI have described an early loss of activity followed by a stage of hyperactivity[43]. Our observation of the transient disappearance of the AIS in layer II/III neurons may suggest that the observed changes in excitability are inherent to the recovery process. Interestingly, the AIS is also a site of neuronal polarization in development and regeneration[44].

Atf3 is not required for mTBI-induced layer V neuron degeneration or death

Although *Atf3* is required for regeneration of sensory neurons following peripheral nerve injury[12,45], our finding that Atf3-GFP cortical neurons in layer V die following mTBI suggested *Atf3* may play a pro-degenerative role in the central nervous system. To investigate this, we deleted *Atf3* in layer V neurons using an Rbp4-Cre driver (Atf3 cKO) and quantified degenerative pathology. We confirmed that layer V ATF3 expression was effectively reduced in Atf3 cKO mice at 7 dpi (Supplementary Fig. 9a,b), with any remaining ATF3+ nuclei likely representing non-neuronal cells. Layer V deletion of *Atf3* did not affect dendrite degeneration[20] or presence of axonal swellings at 7 dpi, nor did it prevent mTBI-induced cell death or microgliosis (Supplementary Fig. 9h-j, 12c,d).

The integrated stress response and SARM1 pathway are not required for mTBI-induced degeneration

Several interconnected signaling pathways influence neurodegeneration (Supplementary Fig. 10a). The integrated stress response (ISR), which halts translation in response to multiple neuronal stressors, and the SARM1 pathway, which controls Wallerian degeneration have both been shown to play neurotoxic roles in mTBI[6,46–50]. We wondered if we could protect layer V neurons by targeting these pathways. We use three genetic models to manipulate key players: a phospho-dead mutant of eIF2α (eIF2a^{S51A}) that results in approximately 50% reduction of eIF2α and thus reduces ISR function[51], a conditional knockout of the pro-apoptotic effector of the ISR *Ddit3* (Ddit3 cKO) in layer V neurons[31], and a global knockout of the executor of Wallerian degeneration Sarm1[52] (Sarm1 KO). We find that targeting each of these pathways on its own is not sufficient to prevent dendrite degeneration, axon beading or swelling, or cell death (Supplementary Fig. 10). Therefore, we conclude that either none of these pathways is important for neuron death following mTBI, or that their collective action is required.

Layer V deletion of Dlk prevents degeneration and death

We had previously noted the upregulation of multiple stress responsive genes in deeper layer cortical neurons (Fig 2g), so it was perhaps unsurprising that deletion of individual pathway effectors was not sufficient to prevent death of layer V neurons. We observed, however, that phosphorylated c-Jun (p-c-Jun), a known binding partner of ATF3, was distributed in a similar pattern as ATF3 in the ipsilateral cortex (Fig. 5a). These transcription factors, ATF3 and p-cJun, are known to be activated by the axon damage sensing protein DLK[53–55] (dual leucine zipper kinase; Supplementary Fig. 10a). DLK can drive ISR activity through phosphorylation of an ISR kinase, PERK[56,57] (Supplementary Fig. 10a, i-k), and promote Sarm1 activation through inhibition of its regulator, NMNAT[58–60] (Supplementary Fig. 10a). We thus reasoned that targeting DLK might be protective as a node sufficiently upstream of multiple neuronal stress responses. Furthermore, while the marker of DLK pathway activation p-c-Jun was detected in both layer V and layer II/III neurons, there was significantly higher expression in layer V neurons, correlating with their differential vulnerability (Fig. 5a,b). We thus tested if deleting DLK would promote survival of Atf3-neurons in layer V.

We conditionally deleted Dlk in layer V neurons using the Rbp4-Cre driver line. We validated that *Dlk* transcript was selectively reduced in layer V DLK cKO neurons (Supplementary Fig. 11b,c). DLK deletion completely prevented layer V neuron death, rescuing the ~15% loss of these neurons in the ipsilateral cortex (Fig. 5c,d). By crossing the DLK cKO line with the Thy1-YFP reporter, we also observed that DLK cKO prevented mTBI-induced dendrite degeneration, and significantly reduced axon beading and swelling (Fig. 5e-g).

DLK signaling is essential in sensory neurons for recruitment of microglia and other inflammatory cells to sites of injury[61–63]. We investigated whether DLK cKO locally reduced microgliosis in the cortex after mTBI. We found that microgliosis was selectively reduced in layer V, where Dlk was

depleted (Supplementary Fig. 12a,b). Interestingly, although DLK is required for *Csf1* upregulation in sensory neurons to recruit microglia following peripheral nerve injury, we found that CSF1 does not play a role in mTBI-induced cortical microgliosis (Supplementary Fig. 12e,f). Thus, mTBI-induced layer V microgliosis is not initiated through a neuronal injury response that actively recruits microglia. Instead, microgliosis may occur as a response to factors released by apoptotic neurons, such as ATP, and prevention of neuron death by DLK deletion is therefore sufficient to prevent microglial recruitment.

We thus find that DLK activation is required for the degeneration of layer V neurons following mTBI, and that its differential activation in layer V and layer II/III neurons may be responsible for the differential vulnerability.

Discussion

In this study, we develop and characterize a model of mild TBI in which we follow the cellular and molecular sequelae of a single impact to the skull on specific cortical neuron types during several weeks following injury. We used a closed-skull injury in order to model a clinically-relevant mild trauma to the cortex. We find that despite its mild nature, this single impact injury produces wide ranging consequences to neurons within the cortex, from cell death to survival, with specific neuron types undergoing specific reproducible fates. We used the neuronal injury marker *Atf3* as a reporter to gain genetic access to a subset of neurons that transcriptionally responds to the injury. This allowed us to molecularly and spatially identify these neurons, describe their location and morphology, record their electrophysiological properties, and determine how their cellular states evolve over time. We discovered that the Atf3-responsive population of neurons falls into two categories: one located in layer V that undergoes neuronal death within 2 weeks after injury, and one in layer II/III that survives at least 2 months after injury. We found that the DLK signaling pathway is responsible for the death of the Atf3-responsive neurons in layer V, highlighting its value as a potential target for prevention treatments for TBI.

One challenge in studying models of mTBI is the ability to accurately quantify events or cell numbers using markers that are transient or altered by the injury itself. For example, commonly used markers to assess apoptosis are quite transient and may be missed. In this study, we demonstrate that many marker genes of cortical neuron types are lost after mTBI, making it impossible to accurately label or quantify the neuronal cell types in which they are normally expressed. This is consistent with other work showing that stress response mechanisms adopted by injured neurons to regain homeostasis after injury often result in the loss of expression of markers genes and proteins[11,12,64]. To overcome this, we relied on genetic labeling to track and record from our neurons of interest. This strategy also facilitated the enrichment of this relatively rare population of cells within the cortex, allowing us to perform single nucleus transcriptomics to molecularly identify them using their transcriptome instead of individual marker genes. Additionally, this novel approach to study injured neurons is applicable to investigating the neuronal Atf3 response in a range of neurodegenerative conditions, beyond TBI.

The Atf3-reporter strategy highlighted the existence of two main populations of neurons after mTBI, and a striking differential vulnerability between them. The neurons in layer V mostly died within 2 weeks of the injury while those in layer II/III survived. An intriguing aspect of the Atf3-GFP neurons in layer II/III is that they initially express the GFP reporter much more weakly than those in layer V. The initially faint reporter labeling may reflect a stronger translational repression in these neurons than in layer V that is reversed as they regain homeostasis. A question naturally arises: what is it about layer V neurons that makes them more vulnerable to degeneration? Layer V neurons have been highlighted as a vulnerable population within the cortex in multiple diseases and experimental models[4,65–69]. Using machine learning to classify the regeneration potential of neurons, a recent study identified layer V neurons as the least regenerative within the cortex[70]. It may be that their large somas, long axons, and metabolic demands require a molecular make-up that confers an increased vulnerability[71]. Selective vulnerability is seen across neurodegenerative diseases, necessitating further research to identify causative elements.

We found that DLK is essential for the death of layer V neurons, consistent with the known role of DLK signaling in promoting neuron death[53,54,72–77]. It is reasonable to imagine that the mild concussive TBI in our model produces axotomy of layer V projection neurons, and thus DLK-dependent death. While some layer II/III neurons have corticocortical projections, others project locally; thus, it is less clear whether they activate the Atf3-stress response pathway as a result of axotomy or another mechanism. Regardless, the majority of these layer II/III neurons do not degenerate within 70 days of the injury. Our snRNAseq data clearly demonstrate that, despite sharing the expression of *Atf3* and *Ecel1*, the neurons from each layer express differential transcriptional programs, consistent with their divergent fates.

Recently, DLK inhibitors have been developed to treat neurodegenerative conditions[54,61,72,78–80], and understanding the role of the DLK pathway in mTBI will be critical for determining if it may be a viable therapeutic target. Recently, a Phase I clinical trial of a DLK inhibitor in ALS patients was halted after weeks of treatment due to observations of adverse effects including low platelet count, ocular toxicity, and altered touch sensation[81]. However, mTBI may be a more appropriate indication for trial as the injury timing can be known or even anticipated and dosing could be acute rather than chronic to reduce undesirable side-effects. Alternate methods to target DLK signaling may also be developed in future.

This study not only deepens our understanding of how cortical neurons respond to mTBI, but also reveals the heterogeneous nature of their responses. By uncovering the differential vulnerability of distinct neuronal populations and their divergent engagement of multiple stress response pathways, we pave the way for targeted therapeutic interventions. It is possible that the initiation of neuronal stress responses after a single acute injury, as described in this study, can make surviving neurons susceptible to further injury, highlighting the need for therapeutic approaches for populations prone to recurrent injury, such as athletes and military personnel. The identification of the DLK pathway as a potential target for neuroprotection opens new avenues for treatment strategies. Ultimately, these findings offer crucial insights into the complex landscape of neuronal injury responses, providing a foundation for future investigations and potential clinical interventions aimed at mitigating the long-term impact of mTBI on cortical neurons.

Methods

Mice

All animal care and experimental procedures were performed in accordance with animal study proposals approved by the *Eunice Kennedy Shriver* National Institute of Child Health and Human Disease Animal Care and Use Committee. Adult (>7 weeks of age) male and female mice were used for all experiments, but were not analyzed separately. Thy1-YFP mice were acquired from The Jackson Laboratory (B6.Cg-Tg(Thy1-YFP)HJrs/J, Jax Stock No. 003782) Atf3-Cre mice, as previously described[11], were generated via knockin of an IRES-Cre sequence after the stop codon of Atf3 at the endogenous locus, such that endogenous Atf3 would remain intact. Atf3-CreER and Atf3 fl/fl mice were obtained from Dr. Clifford Woolf. Dlk fl/fl mice were obtained from Dr. Aaron DiAntonio. For sequencing studies, Atf3-CreER mice were crossed to Sun1-sfGFP (B6;129-Gt(ROSA)26Sortm5(CAG-Sun1/sfGFP)Nat/J, Jax Stock No. 021039) and bred to heterozygosity for both alleles. For visualization of Atf3-expressing neurons, Atf3-Cre or Atf3-CreER mice were crossed to Snap25-LSL-eGFP (B6.Cg-Snap25tm1.1Hze/J, Jax Stock No. 021879) or Ai14 (B6.Cg-Gt(ROSA)26Sortm14(CAG-tdTomato)Hze/J, Jax Stock No. 007914) and bred to heterozygosity for both alleles. For all conditional knockout experiments, Rbp4-Cre mice (Rbp4-Cre (B6.FVB(Cg)-Tg(Rbp4-cre)KL100Gsat/Mmucd, MMRRC Stock No. 037128-UCD) were crossed to the flox line such that the floxed allele would be homozygous and Cre-negative littermates could be used as controls. Chop fl mice (B6.Cg-Ddit3tm1.1Irt/J, Jax Stock No. 030816) and Sarm1 KO (C57BL/6J-Sarm1em1Agsa/J, Jax Sock No. 034399) were used for knockouts. For Sarm1 KO, heterozygote littermates were used as controls, as heterozygous KO is not sufficient to prevent Wallerian degeneration. For ISR manipulation, we used Eif2-S51A mice (B6;129-Eif2s1tm1Rjk/J, Jax Stock No. 017601). Because homozygosity in this mutation is lethal, heterozygotes were used for experiments, and WT littermates were used as controls. For inducible Cre experiments, mice were dosed intraperitoneally with 75 mg/kg of a 20 mg/mL solution of tamoxifen mixed in corn oil at 4 and 5 dpi.

Mild traumatic brain injury

Closed-skull mild traumatic brain injury was administered using the Leica Impact One (Leica Biosystems, Cat. No. 39463920) controlled cortical impact (CCI) device. Mice receiving injury were anesthetized with 2-2.5% isofluorane and positioned in a nose cone on foam pad. No stereotaxic restraint was used, however neonatal ear bars were used to loosely stabilize the head to enhance consistency while maintaining movement upon impact. Mice were shaved and depilated around bregma. The 3 mm piston tip, mounted on the stereotax at an angle of 10 degrees from the vertical plane, was centered roughly at bregma and moved 2 mm lateral to the midline. The impactor was driven at a velocity of 5 m/s, depth of 1.5 mm, and dwell time of 200 ms. Animals receiving sham injuries were shaved, depilated, and anesthetized for the same amount of time as those receiving TBI, but were not administered the injury. Animals were given 5 mg/kg Meloxicam subcutaneously for analgesia immediately after injury and monitored after removal of anesthesia to evaluate righting reflex. Mice exhibiting tissue deformation following injury were excluded.

Serum collection and Neurofilament Light Simoa Assay

Animals were lightly anesthetized using isofluorane until response to painful stimuli was lost. Blood was collected at baseline, 1, 9, and 14 dpi. The retro-orbital sinus of one eye was penetrated with a sterile unfiltered P1000 pipette tip. Blood was collected into BD Microtainer Capillary Blood Collector tubes (Cat. No. 365967) and allowed to clot at room temperature for 10 min. No more than 10% of the animal's body weight by volume was collected per session. Tubes were spun down at 6500 rpm for 10 minutes at 4 °C and the supernatant was aliquoted for storage at -80 °C. The Quanterix Neurology 4-plex A (Item 102153) assay was run following manufacturer instructions. Briefly, standards were plated in triplicate and test samples were plated in duplicate. Only neurofilament-light measurements were detectable and consistent between replicates. The average of the two replicates were reported as the final sample NfL measurement.

Single nucleus RNA isolation and sequencing

Mice were anesthetized using 2.5% avertin and decapitated, and the brain was rapidly dissected. For subdissection, the lateral, anterior, and posterior extents of the tissue were removed, along with everything below the corpus callosum. Ipsilateral and contralateral cortical regions, roughly 4-5 mm diameter, were collected and rapidly frozen in pre-chilled tubes on dry ice, then stored at -80 °C. Nuclei isolation and sequencing was performed as previously described[82]. Ipsilateral cortical regions from 4 animals were pooled for each sequencing run to remove individual variability. Two datasets were integrated for the study, one collected from male animals and one from female animals. Sex differences were not observed. Samples were homogenized in a dounce homogenizer (Kimble Chase 2 ml Tissue Grinder) containing 1 ml freshly prepared ice-cold lysis buffer. The homogenate was filtered through a 40 µm cell strainer (FisherScientific #08-771-1), transferred to a DNA low bind microfuge tube (Eppendorf, #022431048), and centrifuged at 300×g for 5 min at 4 °C. The washing step was repeated, and the nuclei were resuspended in 1× PBS with 1% BSA and 0.2 U/µl SUPERaseIn RNase Inhibitor (ThermoFisher, #AM2696) and loaded on top of a 1.8 M Sucrose Cushion Solution (Sigma, NUC-201). The sucrose gradient was centrifuged at 13,000×g for 45 min at 4 °C for extra cleanup. The supernatant was discarded, the nuclei were resuspended in 1× PBS with 1% BSA, 0.2 U/µl SUPERaseIn RNase Inhibitor, and filtered through a 35 µm cell strainer (Falcon #352235). Before FACS sorting, 5 mM DRAQ5 (ThermoFisher #62251) was added to label nuclei.

GFP+/DRAQ5+ nuclei were sorted and collected on a Sony SH800 Cell Sorter with a 100 mm sorting chip, and 10k GFP+ nuclei were loaded for sequencing. Using a Chromium Single Cell 3′ Library and Gel Bead Kit v3 (10X Genomics), GFP + nuclei were immediately loaded onto a Chromium Single Cell Processor (10X Genomics) for barcoding of RNA from single nuclei. Sequencing libraries were constructed according to the manufacturer's instructions and resulting cDNA samples were run on an Agilent Bioanalyzer using the High Sensitivity DNA Chip as quality control and to determine cDNA concentrations. The samples were combined and run on an Illumina HiSeq2500. There were a total of 370 million reads passing the filter between the two experiments. Reads were aligned and assigned to Ensembl GRm38 transcript definitions using the CellRanger v7.0.1 pipeline (10X Genomics). The transcript reference was prepared as a pre-mRNA reference as described in the Cell Ranger documentation.

Single nucleus RNA sequencing data analysis

Following the CellRanger pipeline, filtered sequencing data were analyzed using the R package Seurat version 4.1.3 following standard procedures. Outliers were identified based on the number of expressed genes and mitochondrial proportions and removed from the data. The data were normalized and scaled with the SCTransform function, dimensional reduction was performed on scaled data, significant principal components (PCs) were identified, and 30 significant PCs were used for downstream clustering. Clustering was performed using the Seurat functions FindNeighbors and FindClusters (resolution = 0.6). Clusters were then visualized with t-SNE or UMAP. Datasets were integrated with the IntegrateData function, and integrated data were then processed by the same methods. Data was visualized with the SCT assay or the RNA assay for dot plots, and plots were generated using Seurat functions. To assign cell types in an unbiased manner, sequenced nuclei were mapped onto a published and annotated mouse motor cortex snRNAseq reference dataset[29,83] using the Seurat MapQuery function. Clusters containing under 20 nuclei were removed from subsequent analyses. Comparisons to the nuclear reference dataset were made by merging it with our sequencing dataset and visualizing the RNA assay.

Fixed tissue harvest and immunostaining

Mice were anesthetized with 2.5% avertin and transcardially perfused with saline, followed by 4% paraformaldehyde. Tissue was post-fixed overnight and cryopreserved in 30% sucrose prior to sectioning. Thirty micrometer thick coronal slices were collected free-floating using a Leica CM3050 S Research Cryostat and stored in antigen preservation solution at 4 °C. For immunostaining, tissue was washed and permeabilized in 0.1% Triton-X100 in 1× PBS (PBSTx), then blocked in 5% normal donkey serum in 0.1% PBSTx. Primary antibodies were diluted in 0.5% normal donkey serum in 0.1% PBSTx and tissue was incubated overnight at 4 °C. Tissue was washed in 0.1% PBSTx and incubated in secondary antibody (ThermoFisher) diluted in 0.1% PBSTx for 1 h, washed in 1× PBS, mounted on positively charged slides, and coverslipped with Prolong Diamond (ThermoFisher #P36961). NeuroTrace (1:500, Life Tech. N21483) was applied following washes for 30 min. Primary antibodies: guinea pig anti-Ankyrin-G (1:500, Synaptic Systems, 386-005), rabbit anti-ATF3 (1:500, Novus Biologicals, NBP1-85816), rat anti-CD68 (1:500, Bio-Rad, MCA1957), rat anti-CTIP2 (1:500, abcam, ab18465), mouse anti-GFAP (1:500, Sigma-Aldrich, G3893), chicken anti-GFP (1:500, Invitrogen, A10262), chicken anti-IBA1 (1:500, Synaptic Systems, 234-006), rabbit anti-phospho-cJun Ser63 (1:300, Cell Signaling Tech., 9261), rabbit anti-phospho-H2AX (1:400, Cell Signaling Tech., 2577), rabbit anti-Olig2 (1:500, Millipore, AB9610). A custom made rabbit anti-β4-Spectrin was shared by Dr. Damaris Lorenzo.

Multiplexed in situ hybridization

Tissue was sectioned coronally at 16 µm onto positively charged slides using a Leica CM3050 S Research Cryostat. Slides were dried in the cryostat, then stored at −80 °C. Multiplexed in situ hybridization was performed according to the manufacturer's instructions for PFA fixed sections (ACD v2 kit). Probe targets were visualized using Opal dyes 520, 570, 690, or 780 (Akoya). Each in situ analysis was performed in at least n = 2 mice. Probes: Atf3 (Cat. No. 426891), Atf4 (Cat.

No. 405101), Ddit3 (Cat. No. 317661), Dlk (Cat. No. 458151), Ecel1 (Cat. No. 475331), Gad2 (Cat. No. 439371), Kcnq5 (Cat. No. 511131), Satb2 (Cat. No. 413261), Scn1a (Cat. No. 556181), Tubb3 (Cat. No. 423391).

Electrophysiology brain slice preparation

Mice were anesthetized using Pentobarbital Sodium (NIH Veterinarian Services) and subsequently decapitated. Brains were swiftly removed and placed in an ice-cold cutting solution containing (in mM): 92 NMDG, 20 HEPES, 25 glucose, 30 NaHCO3, 2.5 KCl, 1.2 NaPO4 saturated, 10 Mg-sulfate, and 0.5 CaCl2 with 95% O2/5% CO2. The solution had an osmolarity of 303-306 mOsm (Wescorp). The extracted brain was promptly blocked, dried on filter paper, and affixed to a platform immersed in ice-cold NMDG-based cutting solution within a chamber of a Leica VT1200 Vibratome. Coronal slices (300 µm thick) encompassing the somatosensory cortex, were cut at a speed of 0.07 mm/s. Post-slicing, sections were incubated in an NMDG-based cutting solution in a chamber for 5-10 min at 34°C. Slices were then transferred to a chamber filled with a modified holding aCSF saturated with 95% O2/5% CO2. The solution contained (in mM): 92 NaCl, 20 HEPES, 25 glucose, 30 NaHCO3, 2.5 KCl, 1.2 NaPO4, 1 mM Mg-sulfate, and 2 mM CaCl2, with an osmolarity of 303-306 mOsm, at room temperature for a minimum of 1 hr. Slices were kept in the holding solution until being transferred to the recording chamber.

Ex-vivo Whole-Cell Electrophysiology

Whole-cell patch-clamp electrophysiology studies were conducted following the methodology previously described[84]. Cells were visualized using infrared-differential interference contrast (IR-DIC) optics on an inverted Olympus BX5iWI microscope. The recording chamber was perfused at a flow rate of 1.5-2.0 ml per minute with artificial cerebrospinal fluid (aCSF) comprising (in mM): 126 NaCl, 2.5 KCl, 1.4 NaH2PO4, 1.2 MgCl2, 2.4 CaCl2, 25 NaHCO3, and 11 glucose (303-305 mOsm), using a pump from World Precision Instruments. For whole-cell recordings of intrinsic excitability, glass microelectrodes (3-5 MΩ) were employed, containing (in mM): 135 K-gluconate, 10 HEPES, 4 KCl, 4 Mg-ATP, and 0.3 Na-GTP. GFP-positive and GFP-negative cells were identified based on the presence or absence of GFP fluorescence in the DIC. Data were filtered at 10 kHz and digitized at 20 kHz using a 1440A Digidata Digitizer (Molecular Devices). Series resistance (<20 MΩ) was monitored with a -5 mV voltage step. Cells exhibiting >20% change in series resistance were excluded from further analysis. For intrinsic excitability, following membrane rupture in voltage clamp, cells were transitioned to the current clamp configuration without holding current injection. Intrinsic excitability was evaluated by applying hyperpolarizing and depolarizing current steps (25 pA steps: 1-sec duration), and changes in voltage and action potential firing were measured. Whole-cell recordings were conducted using a potassium gluconate-based internal solution. For all experiments, cells experiencing a 20% or higher increase in access resistance or high max spike rate consistent with interneurons were excluded from analysis.

Imaging and quantifications

Images were collected using either a Zeiss slide scanner, Zeiss Axiocam 506, or Zeiss confocal LSM800. Images were quantified using FIJI. For cell counts, slide scanner images were cropped to equivalent contralateral and ipsilateral area for 3-4 sections and cells were counted by a blinded observer. For dendrite degeneration quantifications, 63X confocal images were collected from 3-4 sections (3 regions of interest (ROIs) per section per side). A FIJI macro was created to turn each image to binary and use the 'Analyze Particles' feature to collect circular area (circularity >= 0.2) and total area. For axon pathology area measurements, the magic wand tool in the Arivis Vision 4D software was used to manually select all axon blebs (YFP-high, DAPI-negative) for 3-4 sections per animal. Objects with a 3-10 μm^2 area were defined as axon beading, and those with area > 10 μm^2 were defined as axon swellings. For intensity quantifications, Z-planes were summed and ROIs were drawn around cells of interest based on either GFP expression, DAPI expression, or *Tubb3* expression for RNAscope, depending on the analysis. For normalized mean intensity, mean intensities were collected for background ROIs (negative for any signal), and cell mean intensity values were normalized to average background intensity. For percent area quantifications, ROIs were drawn around the ipsilateral or contralateral cortex, a threshold was set and images were turned to binary, then percent area was calculated using the 'Analyze Particles' feature. For all layer-specific quantifications, either DAPI or NeuroTrace was used to determine layers. Layer V was defined as the cortical layer with larger and more dispersed cells. Layer II/III was defined as everything above layer V, and layer VI is everything below.

Statistical analysis

Wherever possible, quantification of microscopy images was performed blinded. Statistical analyses were performed using GraphPad Prism 9. Either ANOVA with Tukey's multiple comparisons test or t-tests were performed.

Acknowledgments

We would like to thank Niamh Crowley for his help with the Quanterix assay, Dr. Vincent Schram and the NICHD Microscopy Core, the NICHD Molecular Genomics Core, Dr. Clifford Woolf and Dr. Aaron DiAntonio for sharing mice, Dr. Damaris Lorenzo for sharing a custom-made antibody, and Drs. Alex Chesler, Mark Cookson, Mark Hoon, Ariel Levine, Tim Petros, and Nick Ryba for helpful discussions about the manuscript. Biorender.com was used to make figure graphics.

'

Author Contributions

MRA and CLP designed the experiments and wrote the manuscript. MRA performed computational analyses. MRA, EYHL, ASG, and HS performed data collection and image analysis. MRA, HAT, and HEY designed whole-cell patch clamp experiments. HEY and VST collected and analyzed electrophysiological recordings.

Funding

CLP is intramurally funded by the National Institutes of Health, ZIA-HD008966 (NICHD).

Data and code availability

The datasets generated in the current study are available from the corresponding author on reasonable request. Data will be deposited to GEO and accession codes will be available before publication. Code used in analyzing nuclear sequencing data will be uploaded to GitHub before publication.

References

1. Maas, A. I. R. *et al.* Traumatic brain injury: integrated approaches to improve prevention, clinical care, and research. *Lancet Neurol.* 16, 987–1048 (2017).

2. McKee, A. C. et al. Chronic Traumatic Encephalopathy in Athletes: Progressive Tauopathy After Repetitive Head Injury. *J Neuropathology Exp Neurology* 68, 709–735 (2009).

3. Kahriman, A. et al. Repeated mild traumatic brain injury triggers pathology in asymptomatic C9ORF72 transgenic mice. *Brain* (2023) doi:10.1093/brain/awad264.

4. Alkaslasi, M. R. et al. Poor Corticospinal Motor *Neuron* Health Is Associated with Increased Symptom Severity in the Acute Phase Following Repetitive Mild TBI and Predicts Early ALS Onset in Genetically Predisposed Rodents. *Brain Sci* 11, 160 (2021).

5. Chiasseu, M., Fesharaki-Zadeh, A., Saito, T., Saido, T. C. & Strittmatter, S. M. Gene-environment interaction promotes Alzheimer's risk as revealed by synergy of repeated mild traumatic brain injury and mouse App knock-in. *Neurobiol. Dis.* 145, 105059 (2020).

6. Chou, A. et al. Inhibition of the integrated stress response reverses cognitive deficits after traumatic brain injury. *P Natl Acad Sci Usa* 114, E6420–E6426 (2017).

7. Sarkar, C. et al. Impaired autophagy flux is associated with neuronal cell death after traumatic brain injury. *Autophagy* 10, 2208–22 (2014).

8. Mierzwa, A. J., Marion, C. M., Sullivan, G. M., McDaniel, D. P. & Armstrong, R. C. Components of Myelin Damage and Repair in the Progression of White Matter Pathology After Mild Traumatic Brain Injury. J Neuropathology Exp Neurology 74, 218–232 (2015).

9. Greer, J. E., McGinn, M. J. & Povlishock, J. T. Diffuse Traumatic Axonal Injury in the Mouse Induces Atrophy, c-Jun Activation, and Axonal Outgrowth in the Axotomized Neuronal Population. *J Neurosci* 31, 5089–5105 (2011).

10. Frankowski, J. C. et al. Brain-wide reconstruction of inhibitory circuits after traumatic brain injury. *Nat Commun* 13, 3417 (2022).

714 11. Nguyen, M. Q., Pichon, C. E. L. & Ryba, N. Stereotyped transcriptomic transformation of
715 somatosensory neurons in response to injury. *Elife* 8, e49679 (2019).

716 12. Renthal, W. et al. Transcriptional Reprogramming of Distinct Peripheral Sensory Neuron
717 Subtypes after Axonal Injury. Neuron (2020) doi:10.1016/j.neuron.2020.07.026.

718 13. Xiong, Y., Mahmood, A. & Chopp, M. Animal models of traumatic brain injury. *Nat Rev*
719 *Neurosci* 14, 128–142 (2013).

720 14. Namjoshi, D. R. et al. Merging pathology with biomechanics using CHIMERA (Closed-Head
721 Impact Model of Engineered Rotational Acceleration): a novel, surgery-free model of traumatic
722 brain injury. *Mol Neurodegener* 9, 55 (2014).

723 15. DeWitt, D. S., Perez-Polo, R., Hulsebosch, C. E., Dash, P. K. & Robertson, C. S. Challenges
724 in the Development of Rodent Models of Mild Traumatic Brain Injury. *J. Neurotrauma* 30, 688–
725 701 (2013).

726 16. Khalil, M. et al. Neurofilaments as biomarkers in neurological disorders. *Nat. Rev. Neurol.* 14,
727 577–589 (2018).

728 17. Porrero, C., Rubio-Garrido, P., Avendaño, C. & Clascá, F. Mapping of fluorescent protein-
729 expressing neurons and axon pathways in adult and developing Thy1-eYFP-H transgenic mice.
730 *Brain Res* 1345, 59–72 (2010).

731 18. Feng, G. et al. Imaging Neuronal Subsets in Transgenic Mice Expressing Multiple Spectral
732 Variants of GFP. Neuron 28, 41–51 (2000).

733 19. Gerdts, J., Sasaki, Y., Vohra, B., Marasa, J. & Milbrandt, J. Image-based Screening Identifies
734 Novel Roles for IκB Kinase and Glycogen Synthase Kinase 3 in Axonal Degeneration. *J Biol*
735 *Chem* 286, 28011–28018 (2011).

736 20. Ahlgren, H. et al. The Nuclear Calcium Signaling Target, Activating Transcription Factor 3
737 (ATF3), Protects against Dendrotoxicity and Facilitates the Recovery of Synaptic Transmission
738 after an Excitotoxic Insult. J Biol Chem 289, 9970–9982 (2014).

739 21. Greer, J. E., Hånell, A., McGinn, M. J. & Povlishock, J. T. Mild traumatic brain injury in the
740 mouse induces axotomy primarily within the axon initial segment. *Acta Neuropathol* 126, 59–74
741 (2013).

742 22. Ziogas, N. K. & Koliatsos, V. E. Primary Traumatic Axonopathy in Mice Subjected to Impact
743 Acceleration: A Reappraisal of Pathology and Mechanisms with High-Resolution Anatomical
744 Methods. J Neurosci 38, 4031–4047 (2018).

745 23. Smith, D. H., Hicks, R. & Povlishock, J. T. Therapy Development for Diffuse Axonal Injury. J.
746 Neurotrauma 30, 307–323 (2013).

747 24. Witcher, K. G. et al. Traumatic brain injury-induced neuronal damage in the somatosensory
748 cortex causes formation of rod-shaped microglia that promote astrogliosis and persistent

749 neuroinflammation. *Glia* 66, 2719–2736 (2018).

750 25. Arlotta, P. et al. Neuronal Subtype-Specific Genes that Control Corticospinal Motor Neuron
751 Development In Vivo. Neuron 45, 207–221 (2005).

752 26. Mo, A. et al. Epigenomic Signatures of Neuronal Diversity in the Mammalian Brain. Neuron
753 86, 1369–84 (2015).

754 27. Thompson, M. R., Xu, D. & Williams, B. R. G. ATF3 transcription factor and its emerging roles
755 in immunity and cancer. *J. Mol. Med.* 87, 1053 (2009).

756 28. Holland, S. D. & Ramer, M. S. Microglial activating transcription factor 3 upregulation: An
757 indirect target to attenuate inflammation in the nervous system. *Front. Mol. Neurosci.* 16, 1150296
758 (2023).

759 29. Yao, Z. et al. A transcriptomic and epigenomic cell atlas of the mouse primary motor cortex.
760 *Nature* 598, 103–110 (2021).

761 30. Kiryu-Seo, S. et al. Neuronal Injury-inducible Gene Is Synergistically Regulated by ATF3, c-
762 Jun, and STAT3 through the Interaction with Sp1 in Damaged Neurons*. J Biol Chem 283, 6988–
763 6996 (2008).

764 31. Syc-Mazurek, S. B., Fernandes, K. A., Wilson, M. P., Shrager, P. & Libby, R. T. Together JUN
765 and DDIT3 (CHOP) control retinal ganglion cell death after axonal injury. Mol Neurodegener 12,
766 71 (2017).

767 32. Sato, M., Chang, E., Igarashi, T. & Noble, L. J. Neuronal injury and loss after traumatic brain
768 injury: time course and regional variability. *Brain Res.* 917, 45–54 (2001).

769 33. Holden, S. S. et al. Complement factor C1q mediates sleep spindle loss and epileptic spikes
770 after mild brain injury. https://www-science-
771 org.ezproxy.nihlibrary.nih.gov/doi/10.1126/science.abj2685 (2021).

772 34. Dmitrieva, N. I. & Burg, M. B. Analysis of DNA breaks, DNA damage response, and apoptosis
773 produced by high NaCl. *Am J Physiol-renal* 295, F1678–F1688 (2008).

774 35. Rogakou, E. P., Nieves-Neira, W., Boon, C., Pommier, Y. & Bonner, W. M. Initiation of DNA
775 Fragmentation during Apoptosis Induces Phosphorylation of H2AX Histone at Serine 139*. *J. Biol.*
776 *Chem.* 275, 9390–9395 (2000).

777 36. Momin, A., Cadiou, H., Mason, A. & McNaughton, P. A. Role of the hyperpolarization-activated
778 current Ih in somatosensory neurons. *J. Physiol.* 586, 5911–5929 (2008).

779 37. Deng, P. & Xu, Z. C. Contribution of Ih to Neuronal Damage in the Hippocampus after
780 Traumatic Brain Injury in Rats. J. Neurotrauma 28, 1173–1183 (2011).

781 38. Kole, M. H. P. et al. Action potential generation requires a high sodium channel density in the
782 axon initial segment. *Nat. Neurosci.* 11, 178–186 (2008).

783 39. Leterrier, C. The Axon Initial Segment: An Updated Viewpoint. *J. Neurosci.* 38, 2135–2145
784 (2018).

785 40. Teliska, L. H., Costa, I. D., Sert, O., Twiss, J. L. & Rasband, M. N. Axon initial segments are
786 required for efficient motor neuron axon regeneration and functional recovery of synapses. J
787 Neurosci 42, JN-RM-1261-22 (2022).

788 41. Marin, M. A. et al. Reassembly of Excitable Domains after CNS Axon Regeneration. J.
789 Neurosci. 36, 9148–9160 (2016).

790 42. Kiryu-Seo, S. et al. Impaired disassembly of the axon initial segment restricts mitochondrial
791 entry into damaged axons. *Embo J* 41, e110486 (2022).

792 43. Carron, S. F., Alwis, D. S. & Rajan, R. Traumatic Brain Injury and Neuronal Functionality
793 Changes in Sensory Cortex. *Frontiers Syst Neurosci* 10, 47 (2016).

794 44. Eichel, K. & Shen, K. The function of the axon initial segment in neuronal polarity. *Dev. Biol.*
795 489, 47–54 (2022).

796 45. Tian, F. et al. Core transcription programs controlling injury-induced neurodegeneration of
797 retinal ganglion cells. Neuron (2022) doi:10.1016/j.neuron.2022.06.003.

798 46. Frias, E. S. et al. Aberrant cortical spine dynamics after concussive injury are reversed by
799 integrated stress response inhibition. *Biorxiv* 2022.05.31.494250 (2022)
800 doi:10.1101/2022.05.31.494250.

801 47. Krukowski, K. et al. Integrated Stress Response Inhibitor Reverses Sex-Dependent
802 Behavioral and *Cell*-Specific Deficits after Mild Repetitive Head Trauma. *J Neurotraum* 37, 1370–
803 1380 (2020).

804 48. Marion, C. M., McDaniel, D. P. & Armstrong, R. C. Sarm1 deletion reduces axon damage,
805 demyelination, and white matter atrophy after experimental traumatic brain injury. Exp Neurol 321,
806 113040 (2019).

807 49. Alexandris, A. S. et al. Traumatic axonopathy in spinal tracts after impact acceleration head
808 injury: Ultrastructural observations and evidence of SARM1-dependent axonal degeneration. Exp
809 Neurol 359, 114252 (2023).

810 50. Henninger, N. et al. Attenuated traumatic axonal injury and improved functional outcome after
811 traumatic brain injury in mice lacking Sarm1. Brain 139, 1094–1105 (2016).

812 51. Costa-Mattioli, M. et al. eIF2α Phosphorylation Bidirectionally Regulates the Switch from
813 Short- to Long-Term Synaptic Plasticity and Memory. Cell 129, 195–206 (2007).

814 52. Waller, T. J. & Collins, C. A. Multifaceted roles of SARM1 in axon degeneration and signaling.
815 *Front. Cell. Neurosci.* 16, 958900 (2022).

816 53. Watkins, T. A. et al. DLK initiates a transcriptional program that couples apoptotic and

817 regenerative responses to axonal injury. *Proc. National Acad. Sci.* 110, 4039–4044 (2013).

818 54. Pichon, C. E. L. et al. Loss of dual leucine zipper kinase signaling is protective in animal
819 models of neurodegenerative disease. *Sci Transl Med* 9, eaag0394 (2017).

820 55. Adib, E. A., Smithson, L. J. & Collins, C. A. An axonal stress response pathway: degenerative
821 and regenerative signaling by DLK. *Curr Opin Neurobiol* 53, 110–119 (2018).

822 56. Farley, M. M. & Watkins, T. A. Intrinsic Neuronal Stress Response Pathways in Injury and
823 Disease. *Annu Rev Pathology Mech Dis* 13, 93–116 (2018).

824 57. Larhammar, M. et al. Dual leucine zipper kinase-dependent PERK activation contributes to
825 neuronal degeneration following insult. Elife 6, e20725 (2017).

826 58. Summers, D. W., Frey, E., Walker, L. J., Milbrandt, J. & DiAntonio, A. DLK Activation
827 Synergizes with Mitochondrial Dysfunction to Downregulate Axon Survival Factors and Promote
828 SARM1-Dependent Axon Degeneration. *Mol Neurobiol* 1–13 (2019) doi:10.1007/s12035-019-
829 01796-2.

830 59. Figley, M. D. & DiAntonio, A. The SARM1 axon degeneration pathway: control of the NAD+
831 metabolome regulates axon survival in health and disease. Curr Opin Neurobiol 63, 59–66 (2020).

832 60. Walker, L. J. et al. MAPK signaling promotes axonal degeneration by speeding the turnover
833 of the axonal maintenance factor NMNAT2. *eLife* 6, e22540 (2017).

834 61. Wlaschin, J. J. et al. Dual leucine zipper kinase is required for mechanical allodynia and
835 microgliosis after nerve injury. Elife 7, e33910 (2018).

836 62. Hu, Z., Deng, N., Liu, K. & Zeng, W. DLK mediates the neuronal intrinsic immune response
837 and regulates glial reaction and neuropathic pain. Exp Neurol 322, 113056 (2019).

838 63. Shin, J. E., Ha, H., Kim, Y. K., Cho, Y. & DiAntonio, A. DLK regulates a distinctive
839 transcriptional regeneration program after peripheral nerve injury. *Neurobiol Dis* 127, 178–192
840 (2019).

841 64. Ogino, Y., Bernas, T., Greer, J. E. & Povlishock, J. T. Axonal injury following mild traumatic
842 brain injury is exacerbated by repetitive insult and is linked to the delayed attenuation of NeuN
843 expression without concomitant neuronal death in the mouse. *Brain Pathol* 32, e13034 (2022).

844 65. Pressl, C. et al. Selective vulnerability of layer 5a corticostriatal neurons in Huntington's
845 disease. Neuron (2024) doi:10.1016/j.neuron.2023.12.009.

846 66. Jara, J. H. et al. Corticospinal Motor Neurons Are Susceptible to Increased ER Stress and
847 Display Profound Degeneration in the Absence of UCHL1 Function. *Cereb. Cortex* 25, 4259–
848 4272 (2015).

849 67. Stone, S. et al. Neuron-specific PERK inactivation exacerbates neurodegeneration during
850 experimental autoimmune encephalomyelitis. *JCI Insight* 4, e124232 (2019).

851 68. Ozdinler, P. H. et al. Corticospinal Motor Neurons and Related Subcerebral Projection
852 Neurons Undergo Early and Specific Neurodegeneration in hSOD1G93A Transgenic ALS Mice.
853 J Neurosci 31, 4166–4177 (2011).

854 69. Maekawa, S. et al. Cortical selective vulnerability in motor neuron disease: a morphometric
855 study. Brain 127, 1237–1251 (2004).

856 70. Kim, H. J. et al. Deep scRNA sequencing reveals a broadly applicable Regeneration Classifier
857 and implicates antioxidant response in corticospinal axon regeneration. Neuron 111, 3953-
858 3969.e5 (2023).

859 71. Yadav, A. et al. A cellular taxonomy of the adult human spinal cord. Neuron 111, 328-344.e7
860 (2023).

861 72. Welsbie, D. S. et al. Functional genomic screening identifies dual leucine zipper kinase as a
862 key mediator of retinal ganglion cell death. *Proc National Acad Sci* 110, 4045–4050 (2013).

863 73. Pozniak, C. D. et al. Dual leucine zipper kinase is required for excitotoxicity-induced neuronal
864 degeneration. *J Exp Medicine* 210, 2553–2567 (2013).

865 74. Welsbie, D. S. et al. Targeted disruption of dual leucine zipper kinase and leucine zipper
866 kinase promotes neuronal survival in a model of diffuse traumatic brain injury. Mol Neurodegener
867 14, 44 (2019).

868 75. Wlaschin, J. J. et al. Promoting regeneration while blocking cell death preserves motor neuron
869 function in a model of ALS. Brain 146, 2016–2028 (2022).

870 76. Saikia, J. M. et al. A critical role for DLK and LZK in axonal repair in the mammalian spinal
871 cord. J Neurosci JN-RM-2495-21 (2022) doi:10.1523/jneurosci.2495-21.2022.

872 77. Miller, B. R. et al. A dual leucine kinase–dependent axon self-destruction program promotes
873 Wallerian degeneration. *Nat Neurosci* 12, 387–389 (2009).

874 78. Siu, M., Ghosh, A. S. & Lewcock, J. W. Dual Leucine Zipper Kinase Inhibitors for the
875 Treatment of Neurodegeneration. *J Med Chem* 61, 8078–8087 (2018).

876 79. Ferraris, D., Yang, Z. & Welsbie, D. Dual leucine zipper kinase as a therapeutic target for
877 neurodegenerative conditions. *Future Med Chem* 5, 1923–1934 (2013).

878 80. Alexandris, A. S. et al. Protective effects of NAMPT or MAPK inhibitors and NaR on Wallerian
879 degeneration of mammalian axons. Neurobiol. Dis. 171, 105808 (2022).

880 81. Katz, J. S. et al. A Phase 1 study of GDC-0134, a dual leucine zipper kinase inhibitor, in ALS.
881 *Ann Clin Transl Neur* 9, 50–66 (2022).

882 82. Alkaslasi, M. R. et al. Single nucleus RNA-sequencing defines unexpected diversity of
883 cholinergic neuron types in the adult mouse spinal cord. Biorxiv 2020.07.16.193292 (2020)
884 doi:10.1101/2020.07.16.193292.

885 83. Hao, Y. et al. Integrated analysis of multimodal single-cell data. Cell 184, 3573-3587.e29
886 (2021).

887 84. Yarur, H. E. et al. Dynorphin / kappa-opioid receptor regulation of excitation-inhibition balance
888 toggles afferent control of prefrontal cortical circuits in a pathway-specific manner. *Mol. Psychiatry*
889 1–13 (2023) doi:10.1038/s41380-023-02226-5.

Figure 1

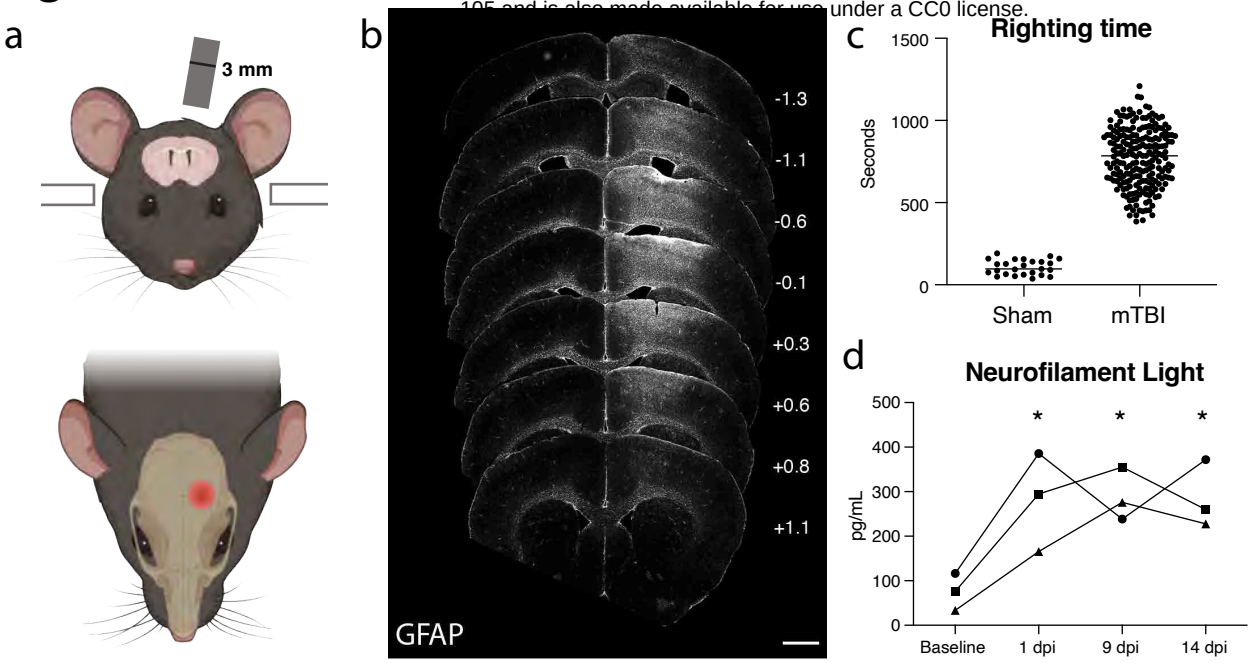

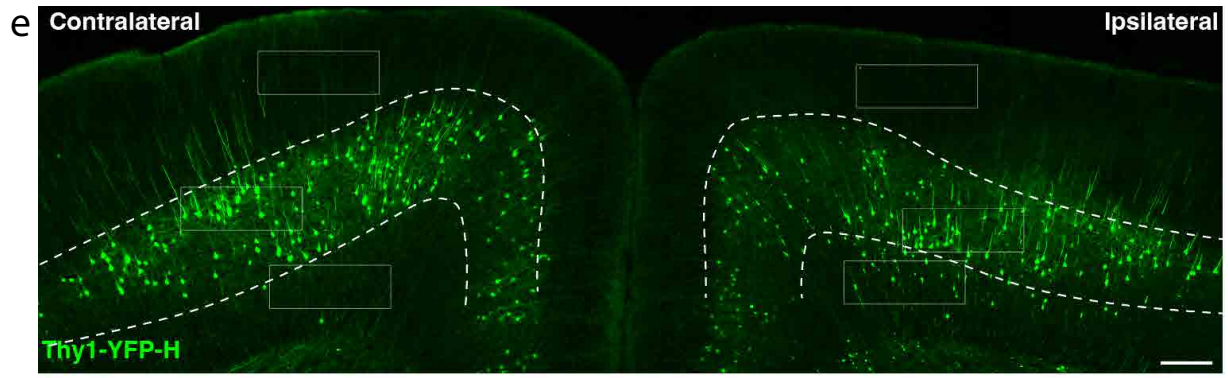

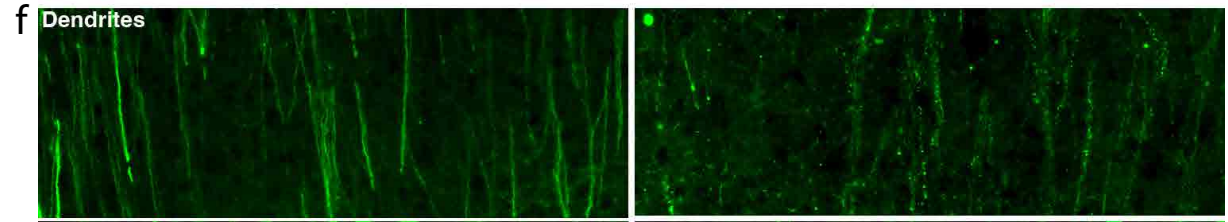

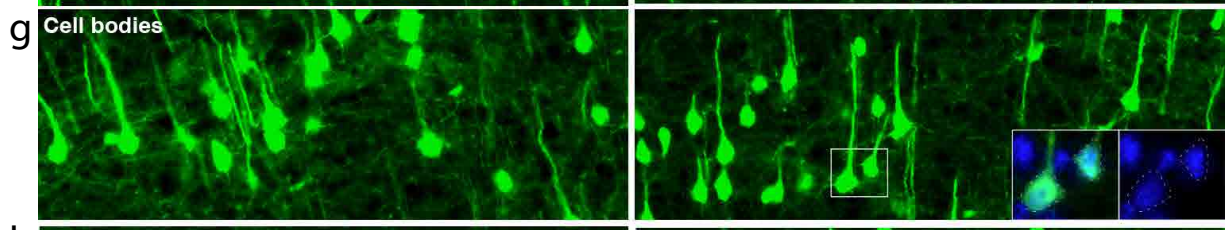

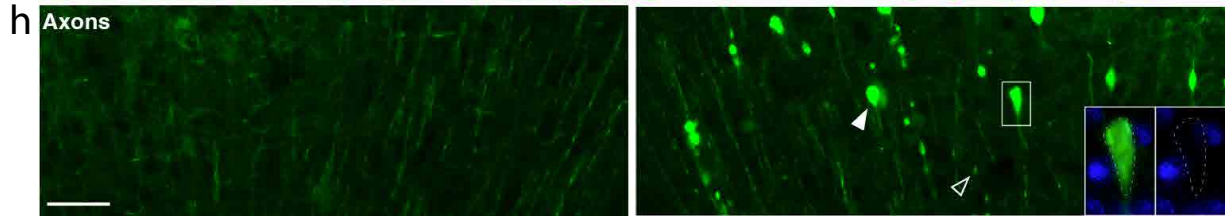

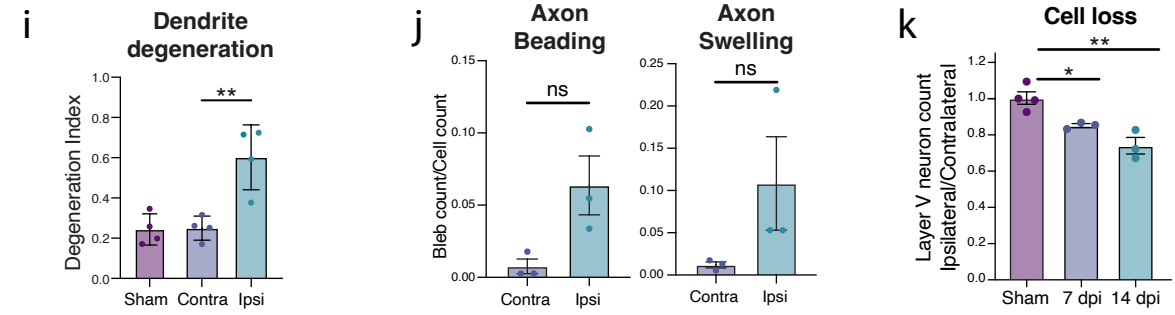

Figure 1. Closed-skull mTBI induces layer V neuron degeneration and death. a. Schematic of injury model and location. A controlled cortical impact injury is delivered lateral to bregma. Coronal view (top) shows 3 mm tip positioned over left cortex. Horizontal view (bottom) shows 3 mm impact site relative to bregma. **b.** Example of extent of injury, representative of > 50 samples in which immunostaining for neuroinflammation was performed. GFAP staining is shown across sections from anterior to posterior. For each section, approximate mm from Bregma on the anterior-posterior axis is shown on the right. **c.** Quantification of righting times (time to wake from anesthesia) demonstrating loss of righting reflex in TBI animals consistent with mild TBI. N = 25 Sham, 218 mTBI. All wildtype mice in the study included, excluding those for which righting time was not accurately recorded. **d.** Longitudinal measurement of neurofilament light in serum of mTBI animals. Points represent the average of two replicates per mouse. **e.** Low magnification image of ipsilateral and contralateral cortex in Thy1-YFP-h mice. Layer V is outlined. High magnification images of **f.** dendrites, **g.** cell bodies, and **h.** axons in the contralateral and ipsilateral cortices. For ipsilateral cell bodies and axons, insets show DAPI expression in cell bodies, and lack of DAPI expression in axon swellings. **i.** Quantification of dendrite degeneration at 7 dpi in ipsilateral, contralateral, and sham. **j.** Quantifications of axon beading (fragments with area < 10 μm^2) and axon swellings (fragments with area > 10 μm^2) at 7 dpi. **k.** Quantification of YFP+ neurons in ipsilateral compared to contralateral cortex in sham animals and at 7 and 14 dpi compared to sham. For **d**, * $P < 0.05$ by Tukey's multiple comparisons test for each timepoint compared to baseline. For **i-k**, points represent the average of 3-4 sections per mouse, * $P < 0.05$, ** $P < 0.005$, ns: not significant, by unpaired t-test. Scale bars: b. 1 mm, e. 200 µm, f-h (shown in h). 50 µm.

Figure 2

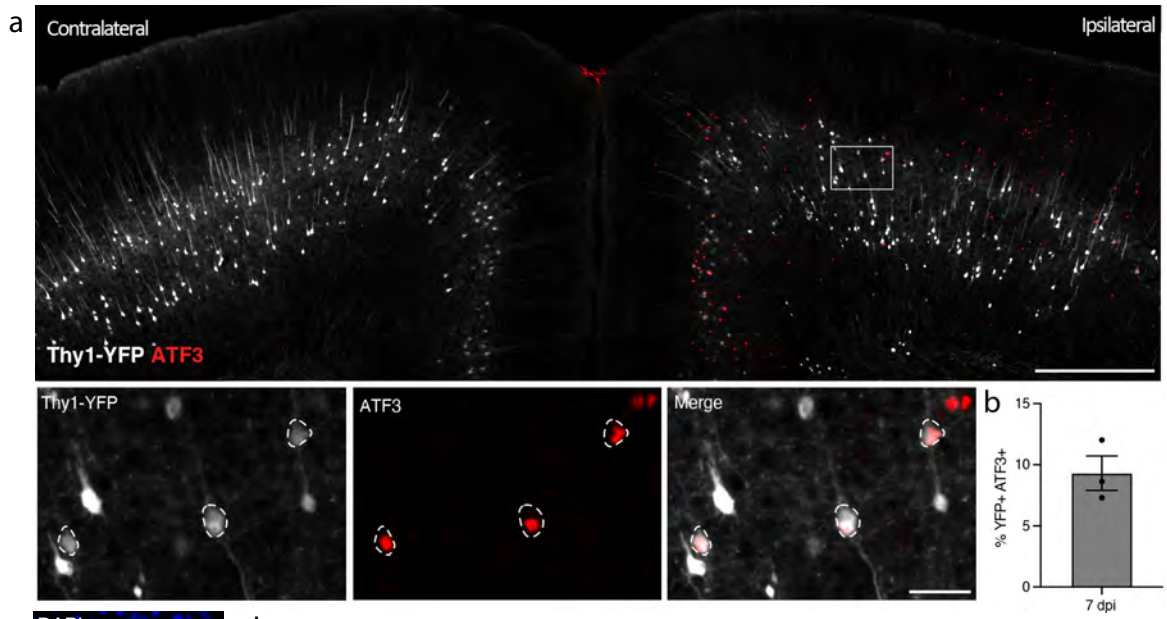

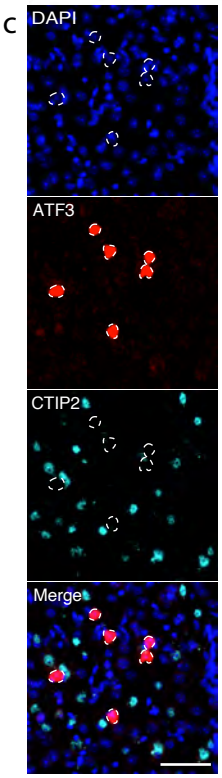

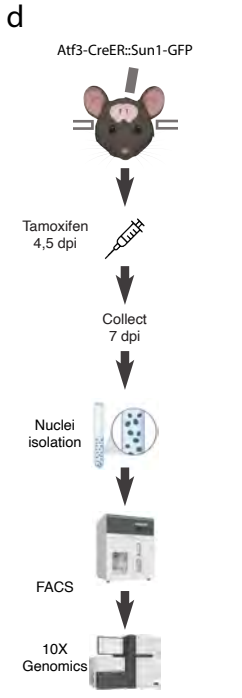

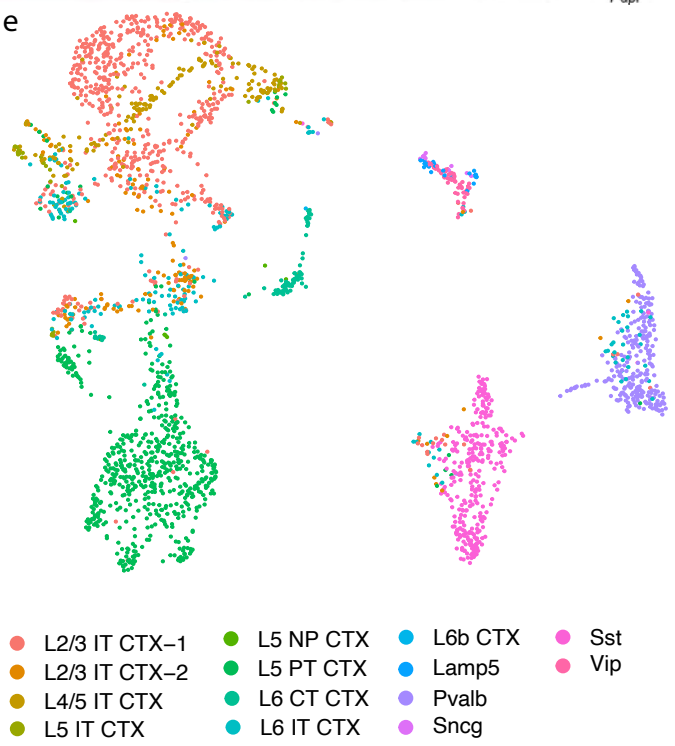

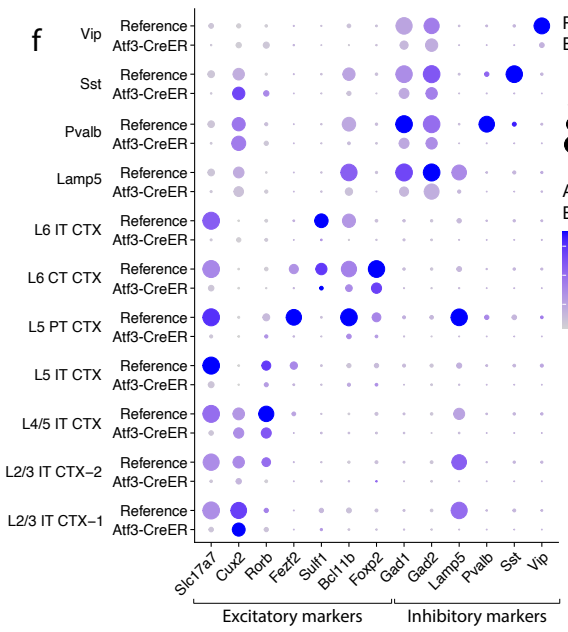

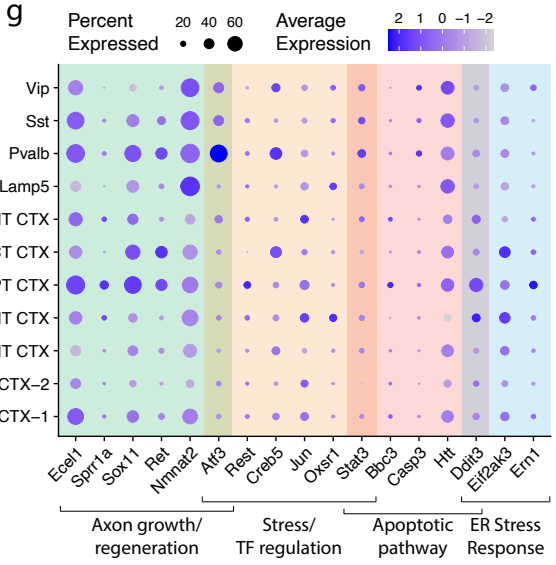

Figure 2. mTBI activates an Atf3-associated transcriptional response in different subtypes of cortical neurons. a. Immunostaining of ATF3 (red) in a Thy1-YFP (white) mouse showing specific expression in the ipsilateral cortex, with higher expression in layer V. Inset highlights YFP+ ATF3+ neurons. ATF3+ neurons are outlined. **b.** Quantification of percent of YFP+ neurons expressing ATF3 at 7 dpi in the ipsilateral cortex. Points represent the average of 3-4 sections per animal. **c.** Immunostaining showing that CTIP2 (cyan) is not expressed in layer V ATF3+ (red) nuclei. ATF3+ nuclei are outlined. **d.** A schematic representation of the single nucleus RNA sequencing workflow, including unilateral closed-skull CCI, tamoxifen dosing, nuclear isolation and FACS, following by 10X Genomics sequencing. **e.** UMAP showing neurons collected by snRNAseq of ipsilateral cortex from pooled Atf3-CreER animals, annotated by mapping to a reference atlas. For subsequent analyses, cell types with fewer than 20 nuclei are excluded. **f.** Dotplot of marker genes for layer-specific excitatory neurons and subtypes of inhibitory neurons, showing downregulation of some markers in Atf3-CreER animals compared to the reference dataset. **g.** Dotplot of a panel of known stress response genes involved in axon growth and regeneration, cell stress and transcription factor regulation, apoptosis, and ER stress highlighting different responses between *Atf3*-expressing neuron subtypes. Genes were selected based on increased expression compared to reference dataset. Low magnification scale bars, 500 μm. High magnification scale bars, 50 μm.

Figure 3

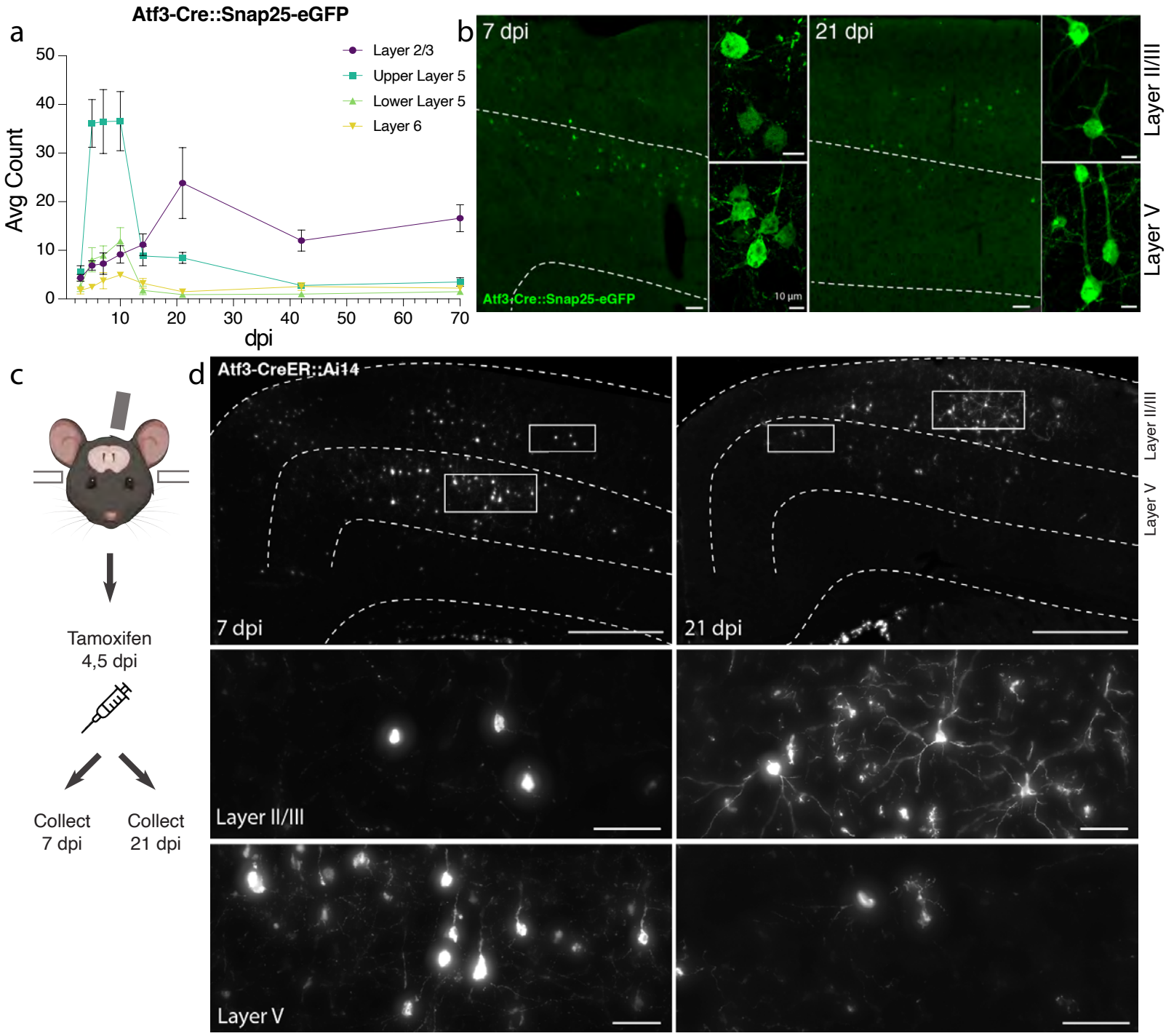

Figure 3. Atf3-expressing neurons in layer V die, while those in layer II/III survive following mTBI . a. Quantification of the average count per section of Atf3-GFP neurons by cortical layer at 3, 5, 7, 10, 14, 21, 42, and 70 dpi. N=6 per timepoint, 3-4 sections counted per animal. **b.** Examples of Atf3-GFP endogenous labeling (left) at 7 and 21 dpi. Layer V is outlined. High magnification examples of GFP-immunolabeled neurons (right) in layer II/III (top) and layer V (bottom) at 7 and 21 dpi. **c.** Schematic representation of tamoxifen dosing and tissue collection. The Atf3-CreER mouse was crossed to the Ai14 RFP reporter (not neuron-specific). **d.** Representative images of Ai14 signal in ipsilateral cortex at 7 dpi and 21 dpi. Layer V is outlined. Insets highlight neurons and other labeled cells in layer II/III and layer V. Insets for layer II/III suggest an earlier loss of projection complexity that is regained by 21 dpi. Inset for layer V at 21 dpi includes a neuron (left) and a microglion (right). For **a**, error bars represent standard error of the mean (SEM). Scale bars: b. Low magnification, 50 µm, high magnification, 10 µm; d. Low magnification, 500 µm, high magnification, 50 µm.

Figure 4

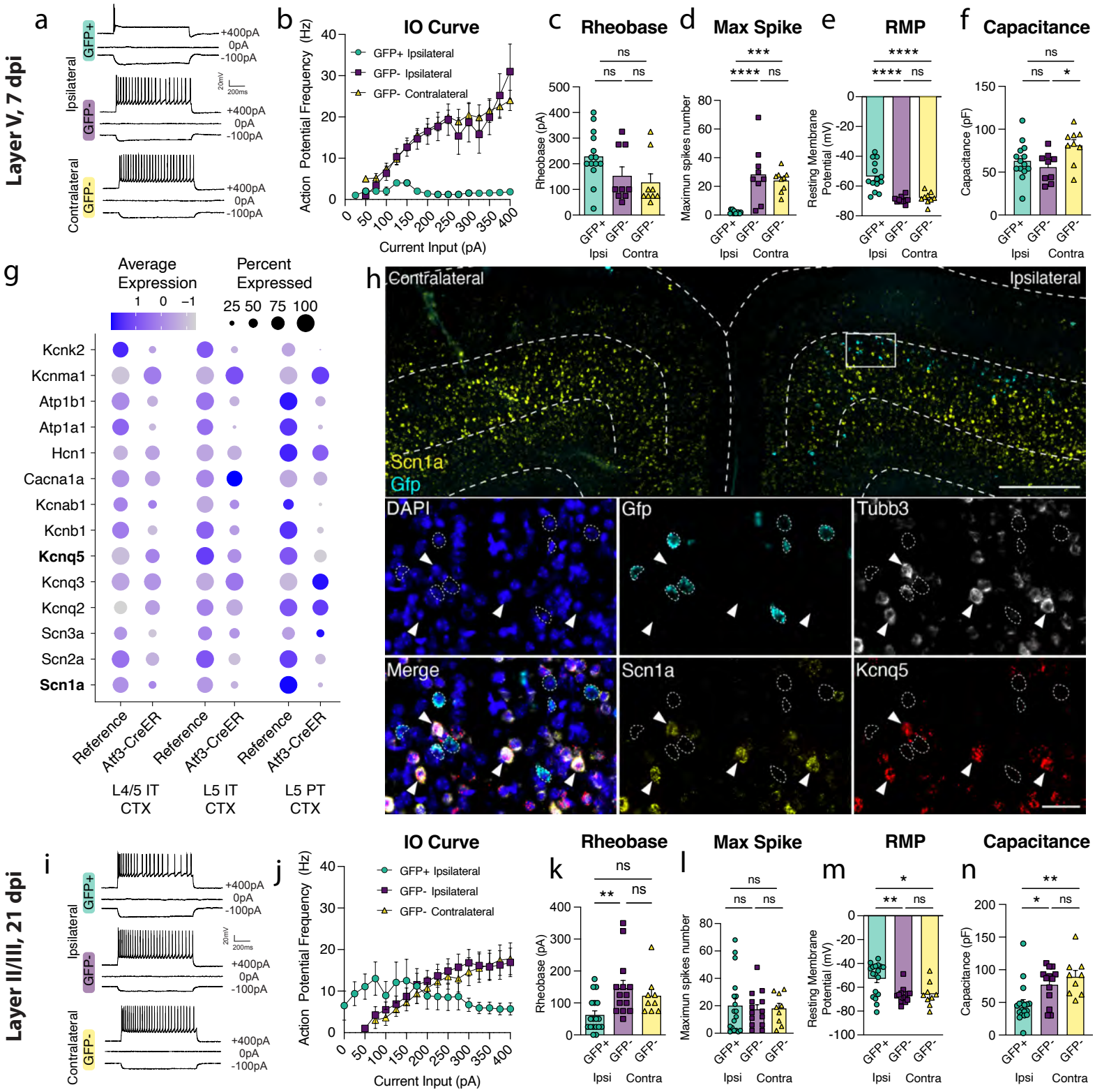

Figure 4. Layer V Atf3-GFP neurons are unable to fire and downregulate ion channels while layer II/III Atf3-expressing neurons are electrophysiologically functional following mTBI. a. Examples of electrophysiological traces from 7 dpi layer V ipsilateral GFP+ and GFP- neurons and contralateral GFP- neurons. Quantifications of **b.** IO curve, **c.** rheobase, **d.** max spike count, **e.** resting membrane potential, and **f.** capacitance in 7 dpi layer V neurons. **g.** Dot plot of select ion channels in the reference dataset compared to the Atf3-CreER dataset collected in this study showing dysregulation of ion channels in layer V neurons. Genes in bold were validated by *in situ* hybridization. **h.** In situ hybridization validating downregulation of ion channels. Low magnification image of bilateral cortices from an Atf3-Cre::Snap25-GFP mouse at 7 dpi showing mRNA expression of *Gfp* (cyan) and *Scn1a* (yellow). Layer V is outlined. Inset shows mRNA of *Gfp* (cyan), *Tubb3* (white), *Scn1a* (yellow), and *Kcnq5* (red). *Gfp*+ neurons (outlined) lack expression of *Scn1a* and *Kcnq5* and have little to no expression of *Tubb3*. Arrowheads highlight *Tubb3*+ *Gfp*- neurons with high expression of *Scn1a* and *Kcnq5*. A single Z-plane is shown in the insets. **i.** Examples of electrophysiological traces from 21 dpi layer II/III surviving ipsilateral GFP+ and GFP- neurons and contralateral GFP- neurons. Quantifications of **j.** IO curve, **k.** rheobase, **l.** max spike count, **m.** resting membrane potential, and **n.** capacitance in 21 dpi layer II/III neurons. For **b** and **j**, points represent the average of all neurons per group, error bars represent SEM. For **c-f** and **k-n**, each point represents one neuron recorded from N = 2-3 animals. * $P < 0.05$, ** $P < 0.005$, *** $P < 0.0005$, **** $P < 0.0001$, ns: not significant, by Tukey's multiple comparisons test. Low magnification scale bar, 50 µm. High magnification scale bar, 500 µm.

Figure 5

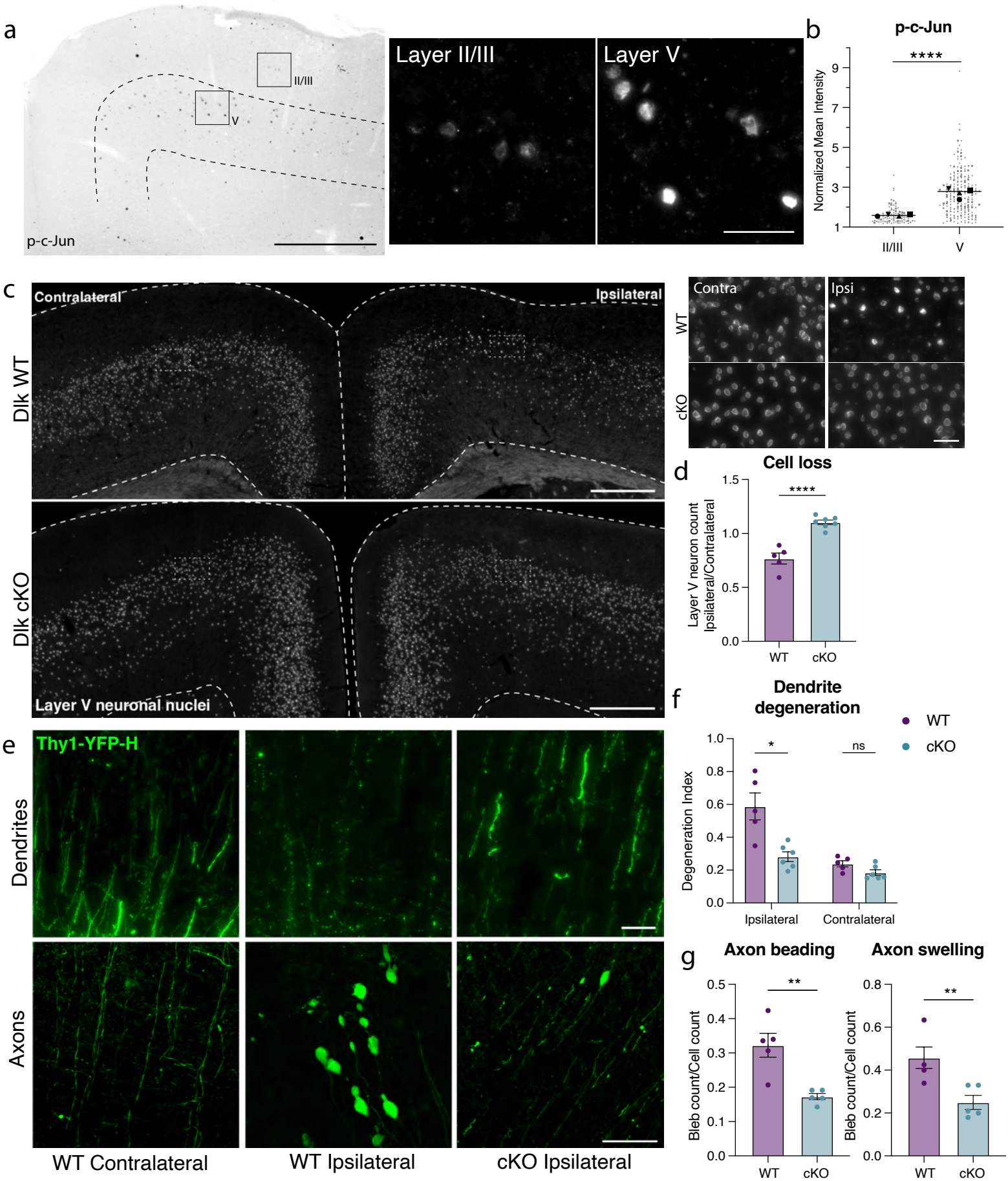

Figure 5. Layer V neurons can be rescued from mTBI-induced death and degeneration by deletion of DLK. a. P-c-Jun immunolabeling in the ipsilateral cortex of WT mice at 7 dpi (left). Layer V is outlined. Insets show high magnification images of immunolabeling in layer II/III and layer V. **b.** Quantification of p-c-Jun intensity in layer II/III and layer V at 7 dpi. Only p-c-Jun+ cells are included based on a threshold of 1.2-fold expression compared to background. Average per animal and value per cell are displayed. Each shape represents one animal. N=4, 2 sections per animal, 11-53 nuclei per animal. **c.** Overview of ipsilateral and contralateral cortices in DLK WT and DLK cKO mice showing layer V GFP+ nuclei. Insets shown on the right. **d.** Quantification of GFP+ neurons in ipsilateral compared to contralateral cortex in WT and cKO mice at 14 dpi based on Sun1-GFP expression shown in c. **e.** High magnification images of YFP+ dendrites (top) and axons (bottom) in WT contralateral and ipsilateral cortex, and cKO ipsilateral cortex. **f.** Quantification of dendrite degeneration at 7 dpi in WT and cKO mice. **g.** Quantification of axon beading and swelling at 7 dpi in WT and cKO mice. For **d**, **f**, **g**, each point represents the average of 3-4 sections per animal. * $P < 0.05$, ** $P < 0.005$, **** $P < 0.0001$, by unpaired t-test. Low magnification scale bars, 50 µm. High magnification scale bars, 500 µm.

Supplemental Figure 1

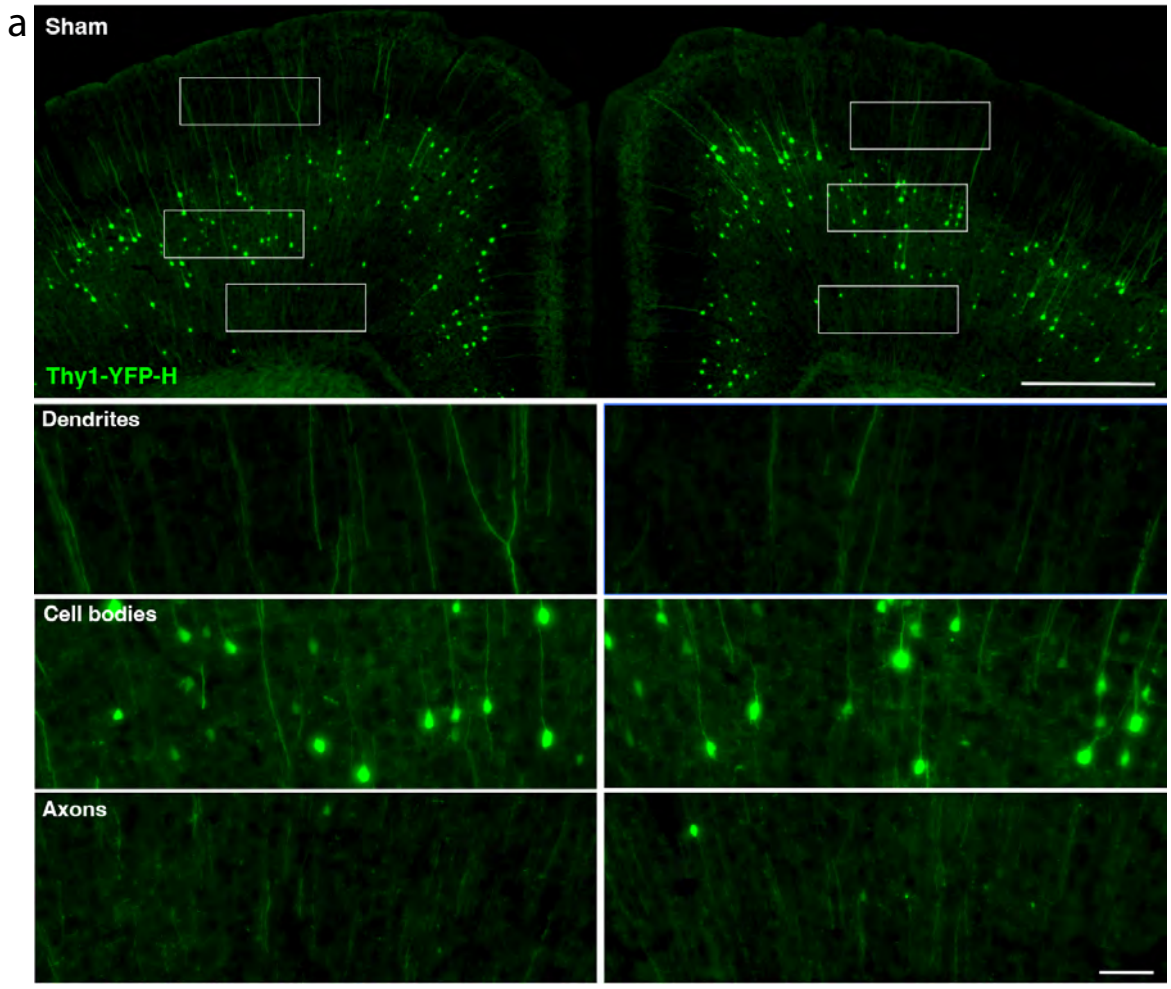

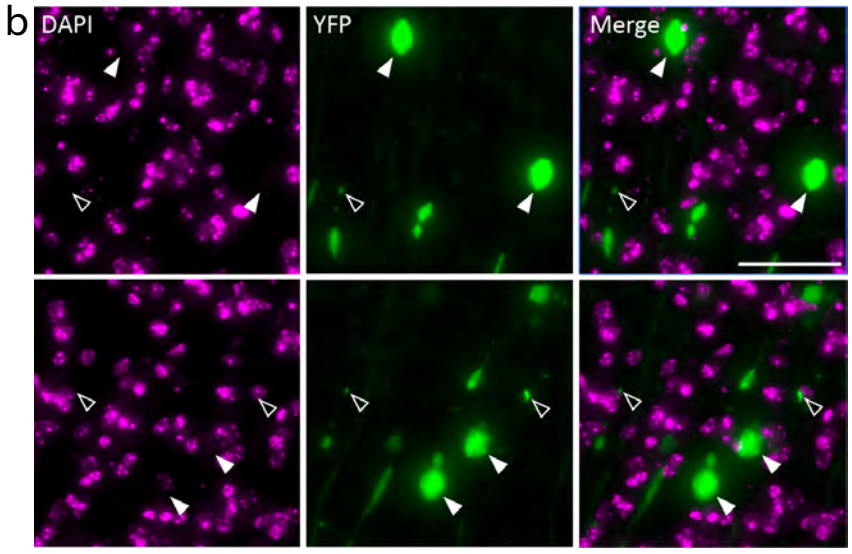

Supplemental Figure 1. Thy1-YFP expression in sham and classification of axon blebs. a. Example coronal section from an uninjured sham Thy1-YFP animal with dendrites, cell bodies, and axons highlighted below. Scale bar representative for all insets. **b.** High magnification images showing DAPI expression and the axons of Thy1-YFP animals after mTBI. Closed arrows highlight DAPI-negative axonal swellings, open arrows highlight axon beading. Lack of DAPI-staining was an inclusion criterion for axon swellings. Low magnification scale bar, 500 µm. High magnification scale bar, 50 µm.

Supplemental Figure 2

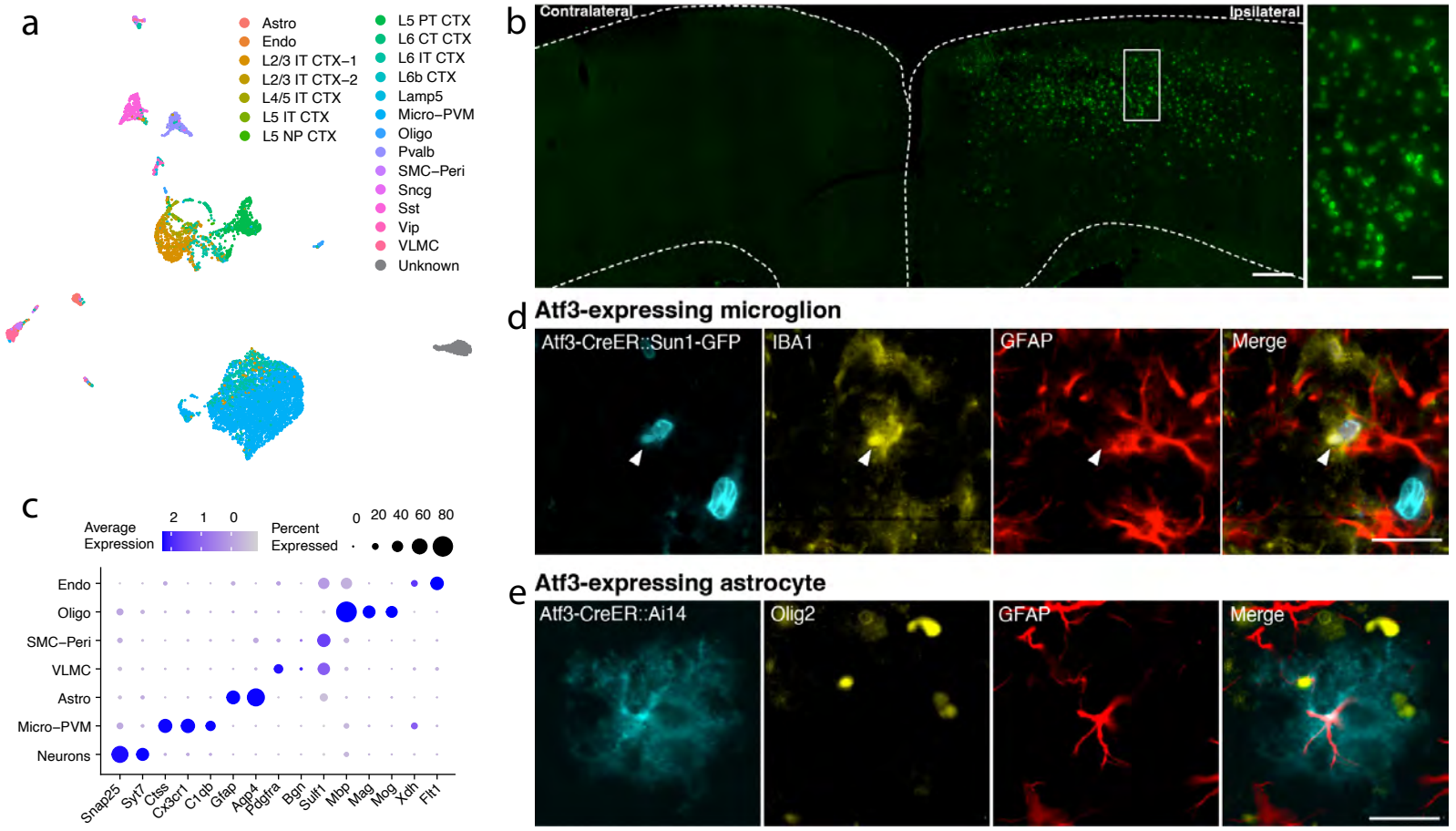

Supplemental Figure 2. Validation of Atf3-expressing cell types. a. UMAP of all *Atf3*-expressing cells collected at 7 dpi from the Atf3-CreER mouse, annotated by mapping to a reference atlas. One neuronal cluster could not be confirmed as cortical, labeled as "Unknown". **b.** Coronal section of cortex showing expression of Atf3-CreER::Sun1-GFP in mice used for sequencing (tamoxifen at 4 and 5 dpi, tissue collected at 7 dpi). Inset highlights large and small nuclei in cortical layers V and II/III. **c.** Dotplot of general cell type markers confirming the reference mapping shown in a. **d.** Validation of the existence of Atf3-expressing microglia seen in the sequencing. Atf3-CreER::Sun1-GFP signal highlights an Atf3-expressing nucleus (cyan) expressing IBA1 (yellow), but not GFAP (red). **e.** Validation of the existence of Atf3-expressing astrocytes seen in the sequencing. Atf3-CreER::Ai14 signal highlights an Atf3-expressing astrocyte (cyan) expressing GFAP (red), but not Olig2 (yellow). Low magnification scale bar, 200 µm. High magnification scale bar, 25 µm.

Supplemental Figure 3

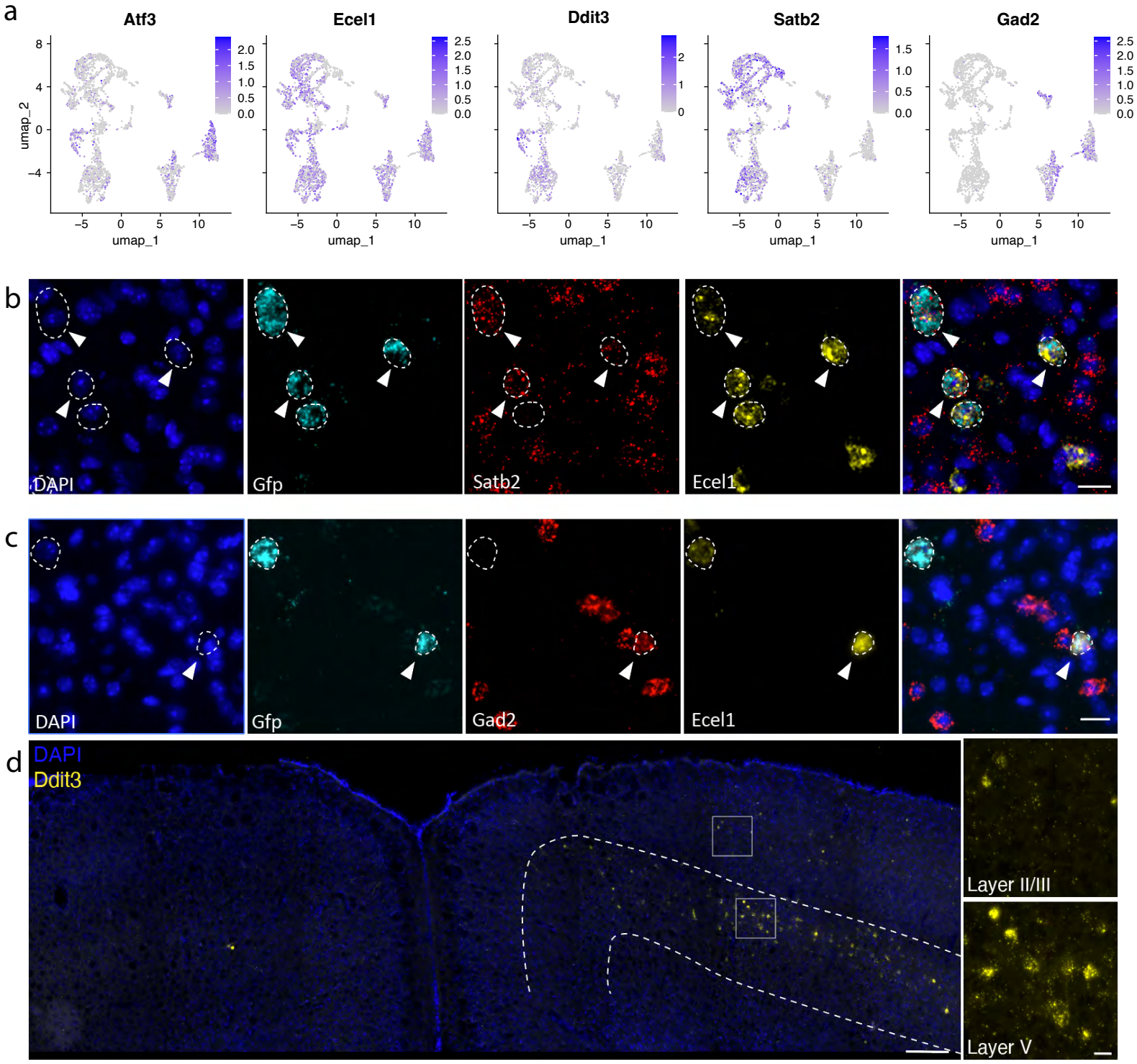

Supplemental Figure 3. Validation of Atf3-expressing neuron types. a. Feature plots of *Atf3, Ecel1, Ddit3* and markers for Atf3-expressing neuron groups; *Satb2* for injured excitatory neurons, *Gad2* for inhibitory neurons. **b.** ISH highlighting injured excitatory neurons, showing coexpression of *Ecel1* (yellow) and *Satb2* (red) in *Gfp*+ cells (cyan) in the Atf3-CreER::Sun1-GFP injured cortex at 7 dpi. *Gfp*+ cells are outlined. Arrowheads pointing at *Gfp*+ injured excitatory neurons. **c.** ISH highlighting injured inhibitory neurons, showing coexpression of *Ecel1* (yellow) and *Gad2* (red) in *Gfp*+ cells (cyan) in the Atf3-CreER::Sun1-GFP injured cortex at 7 dpi. *Gfp*+ cells are outlined. Arrowhead points to a *Gfp*+ injured inhibitory neuron. **d.** ISH of *Ddit3* (yellow) shown in ipsilateral and contralateral cortices. Layer V is outlined. Insets highlight ipsilateral neurons in layer II/III (top) and layer V (bottom). Scale bars, 20 µm.

Supplemental Figure 4

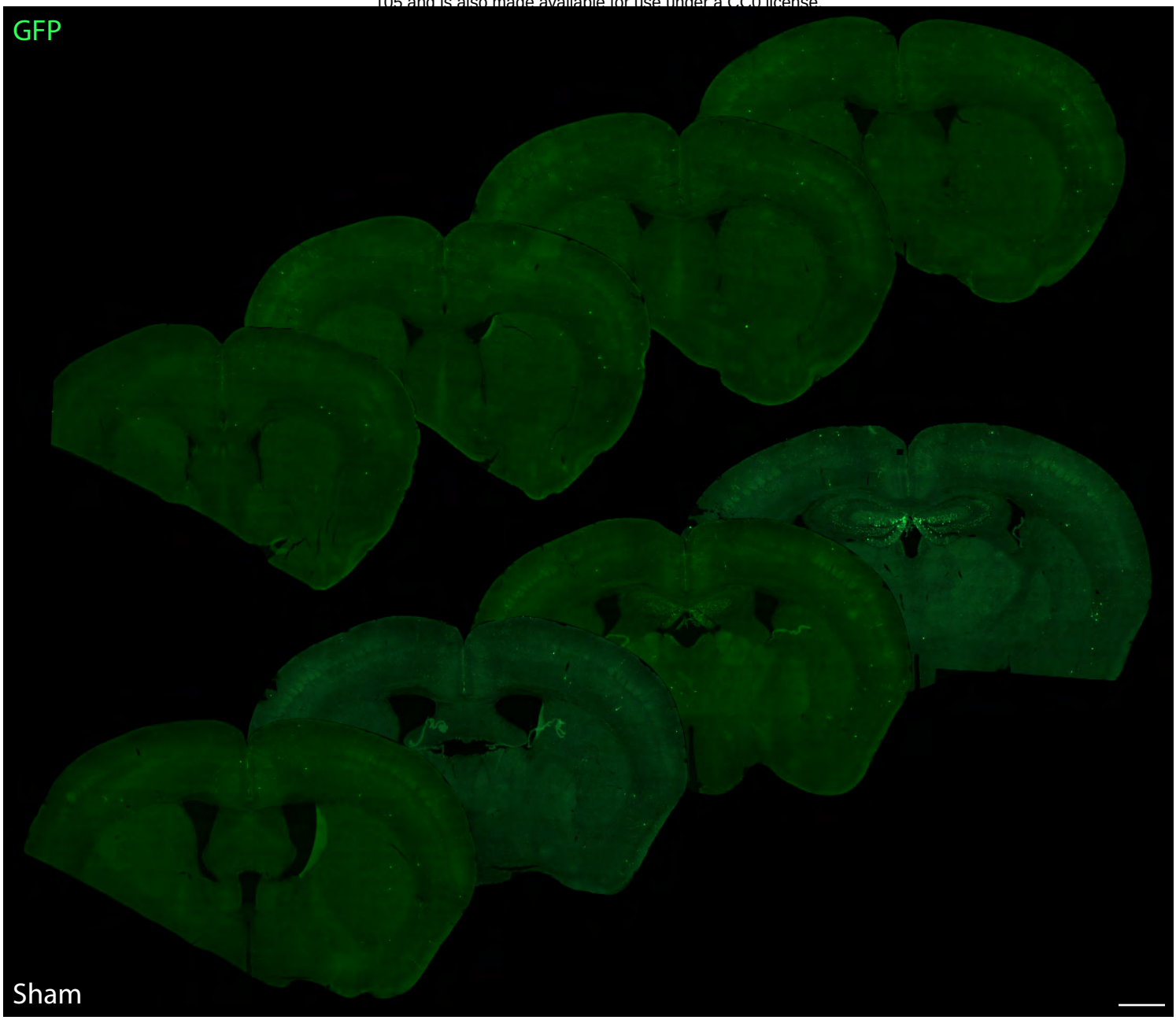

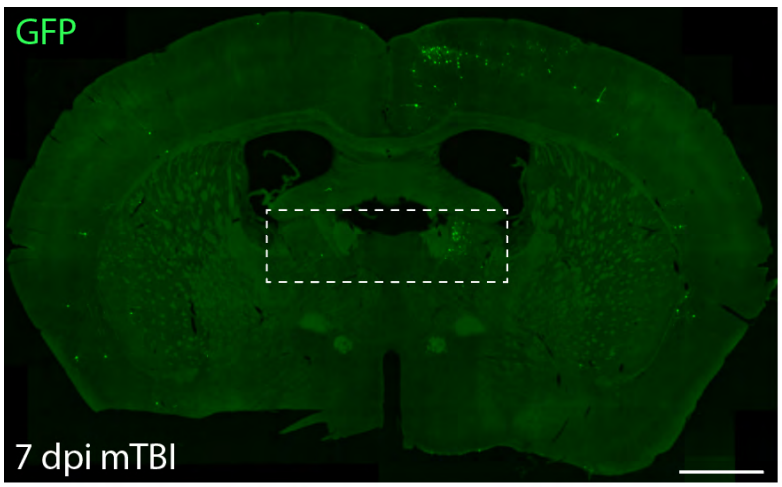

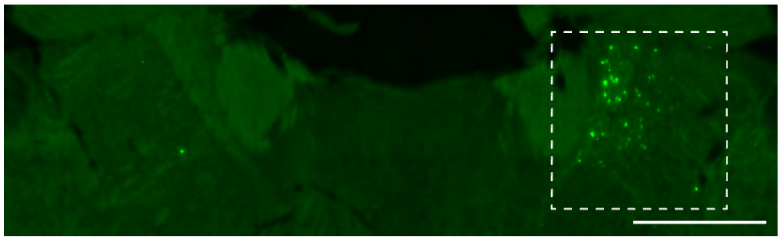

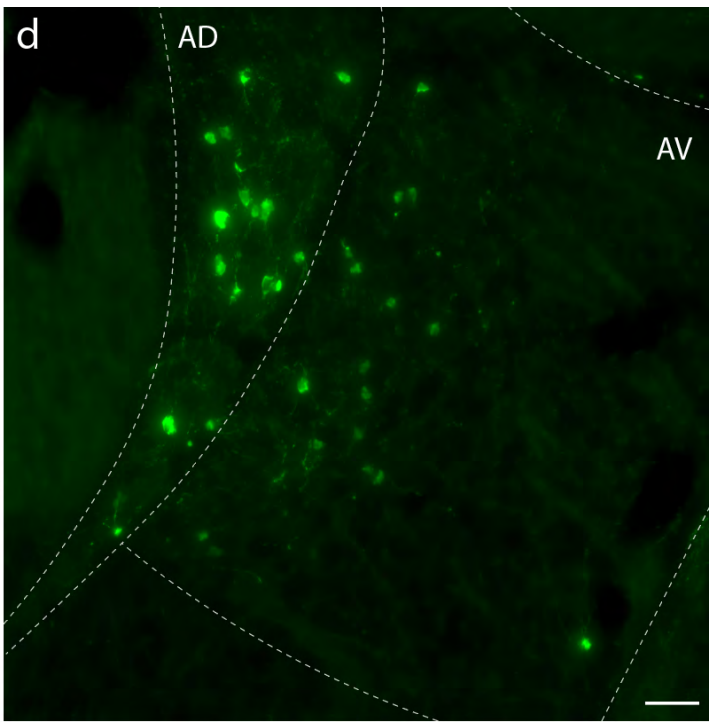

Supplemental Figure 4. Atf3-Cre::Snap25-GFP expression at 7 dpi. a. Coronal sections from Atf3-Cre::Snap25-GFP sham animals (uninjured) showing immunolabeling of GFP without injury. Many hippocampal neurons express GFP, likely due to developmental Atf3 expression. The right ventral portion of the brain was notched. **b.** Image showing a section with GFP immunolabeling at 7 dpi in the ipsilateral cortex and ipsilateral anterior thalamic nuclei. **c.** Inset shows bilateral anterior thalamic nuclei, with GFP immunolabeling in the ipsilateral nuclei. **d.** Inset of the ipsilateral anterior thalamic nuclei. The anterodorsal (AD) and anteroventral (AV) thalamic nuclei are outlined. Low magnification scale bars, 1 mm. Scale bars in **b** and **c**, 500 µm. Scale bar in **d**, 50 µm.

Supplemental Figure 5

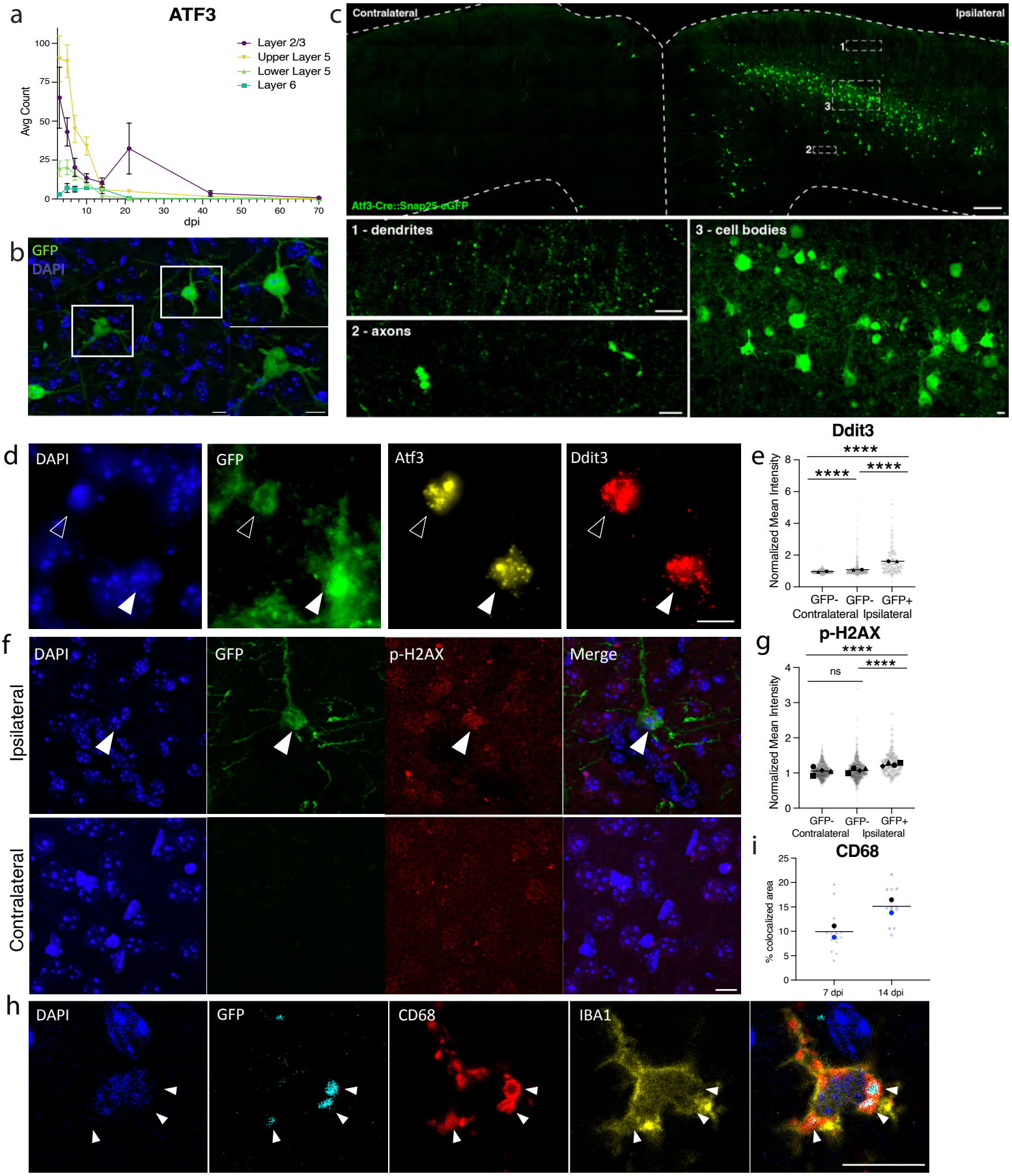

Supplemental Figure 5. Layer V Atf3-GFP neurons undergo apoptosis by 14 dpi. a. Quantification of ATF3 protein expression (regardless of cell type) by cortical layer at 3, 5, 7, 10, 14, 21, 42, and 70 dpi. N=6 per timepoint, 3-4 sections counted per animal. Error bars represent SEM. **b.** High magnification image of layer V GFP-expressing neurons highlighting a neuron that appears morphologically healthy (top) and one that appears unhealthy (bottom). **c.** Low magnification image of ipsilateral and contralateral cortex in Atf3-Cre::Snap25-eGFP mice. High magnification images of dendrite region (1) highlighting degeneration, axon region (2) highlighting axon swellings, and cell body region (3) highlighting variability in neuron morphology. **d.** *In situ* hybridization of *Atf3* and *Ddit3* in Atf3-GFP tissue highlighting layer V GFP+ neurons that appear morphologically unhealthy and co-express these genes. Open arrowhead highlights neuron with condensed DAPI, closed arrowhead highlights neuron with low GFP expression. **e.** Quantification of mean intensity of *Ddit3* mRNA in layer V GFP+ neurons and GFP- neurons of the ipsilateral and contralateral cortices at 7 dpi normalized to background intensity. Average per animal and value per cell are displayed. Each shape represents one animal. **f.** Immunostaining of phospho-H2AX in Atf3-GFP tissue in ipsilateral (top) and contralateral (bottom) cortex. Arrow highlights a layer V GFP+ neuron that appears vacuolized and expresses high levels of phospho-H2AX. **g.** Quantification of mean intensity of phospho-H2AX in the nuclei of GFP+ neurons and GFP- neurons in the ipsilateral and contralateral cortices in layer V at 7 dpi normalized to background intensity. Average per animal and value per cell are displayed. Each shape represents one animal. **h.** High magnification of a microglion (IBA1, yellow) at 7 dpi. Arrows highlight microglial lysosomes (CD68+, red) engulfing GFP+ debris (cyan). **i.** Quantification of percent of CD68+ area colocalized with GFP, reflecting CD68 engulfment of GFP+ debris at 7 and 14 dpi. Average per animal and value per ROI are displayed. Each color represents one animal. **** $P < 0.0001$, Tukey's multiple comparisons test, based on measure of each cell. Scale bars, 10 µm.

Supplemental Figure 6

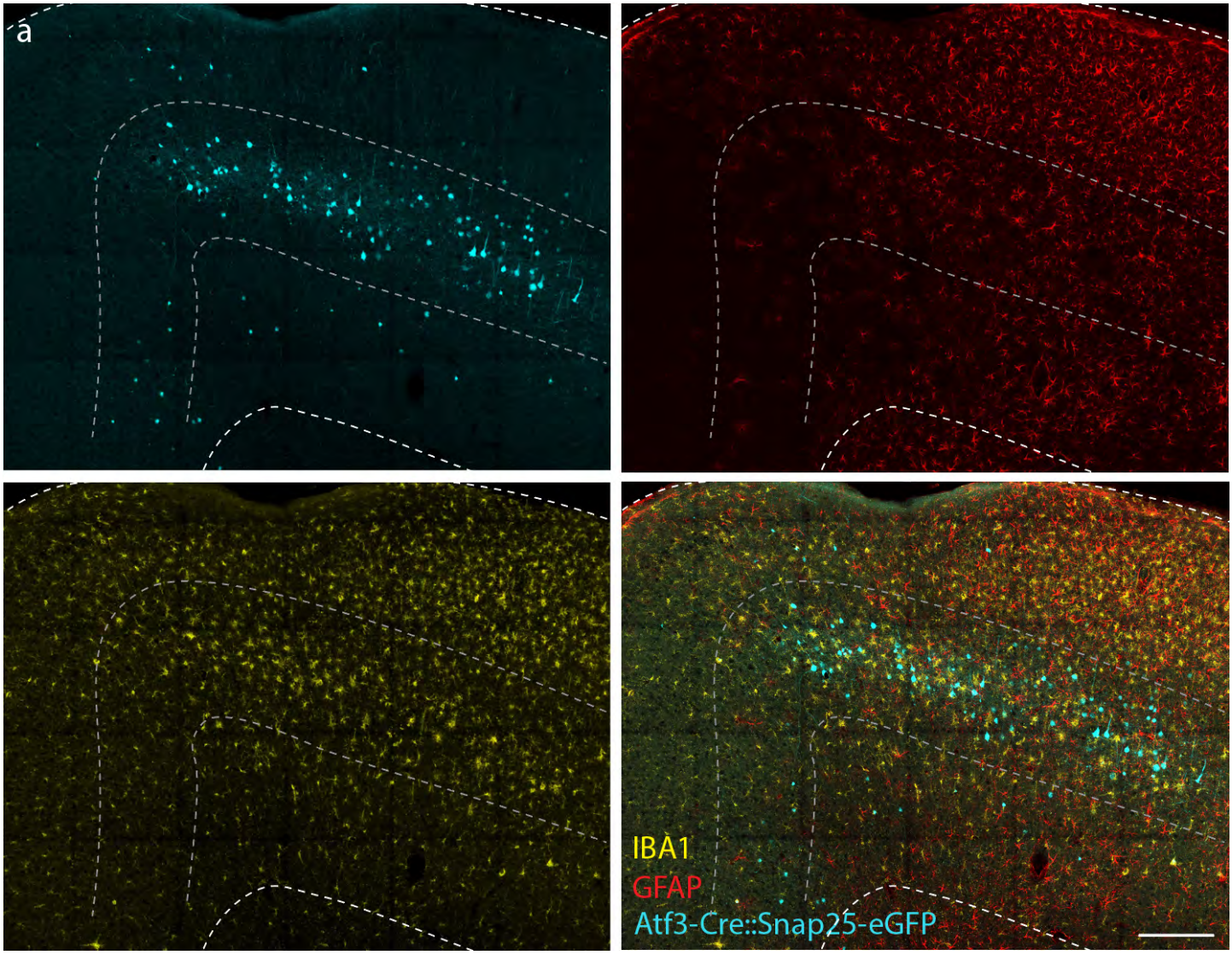

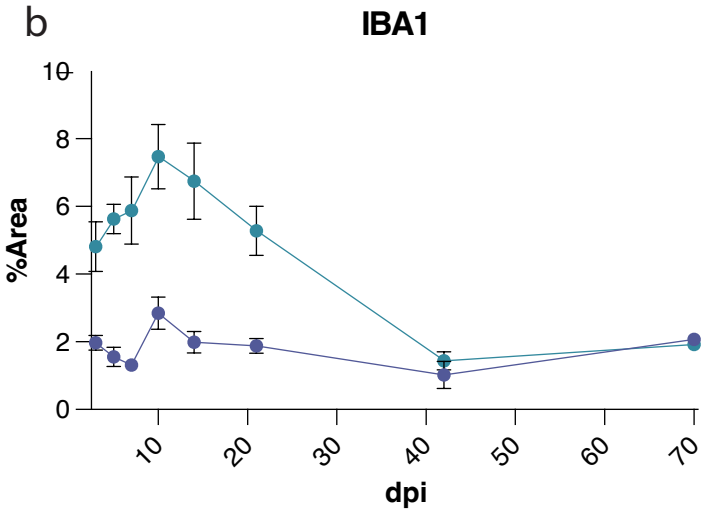

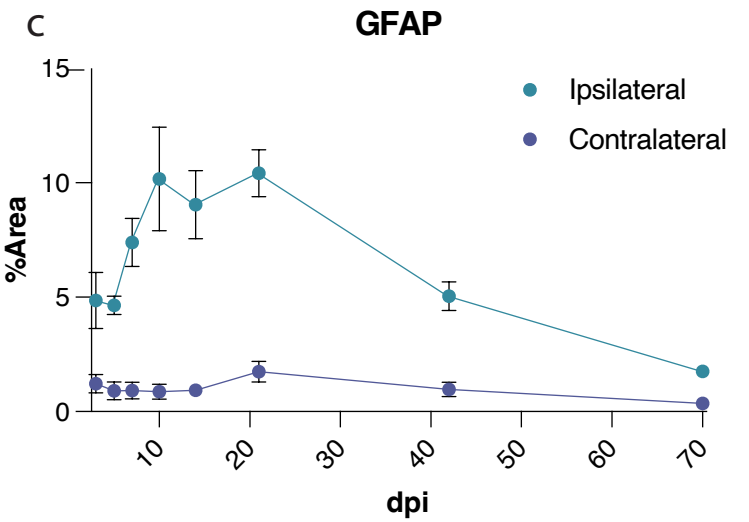

Supplemental Figure 6. Neuroinflammation timecourse following mTBI. a. Immunostaining for IBA1 (yellow) and GFAP (red) in ipsilateral cortex of Atf3-Cre::Snap25-eGFP tissue, highlighting the double layer pattern of microgliosis around GFP+ neurons (cyan) and the injury site and the extent of astrogliosis throughout the injured cortex. Layer V is outlined. **b.** Quantification of percent area of IBA1 expression in the ipsilateral compared to contralateral cortex. **c.** Quantification of percent area of GFAP expression in the ipsilateral compared to contralateral cortex. N=6 per timepoint, 3-4 sections counted per animal. Error bars represent SEM. Scale bar, 200 µm.

Supplemental Figure 7

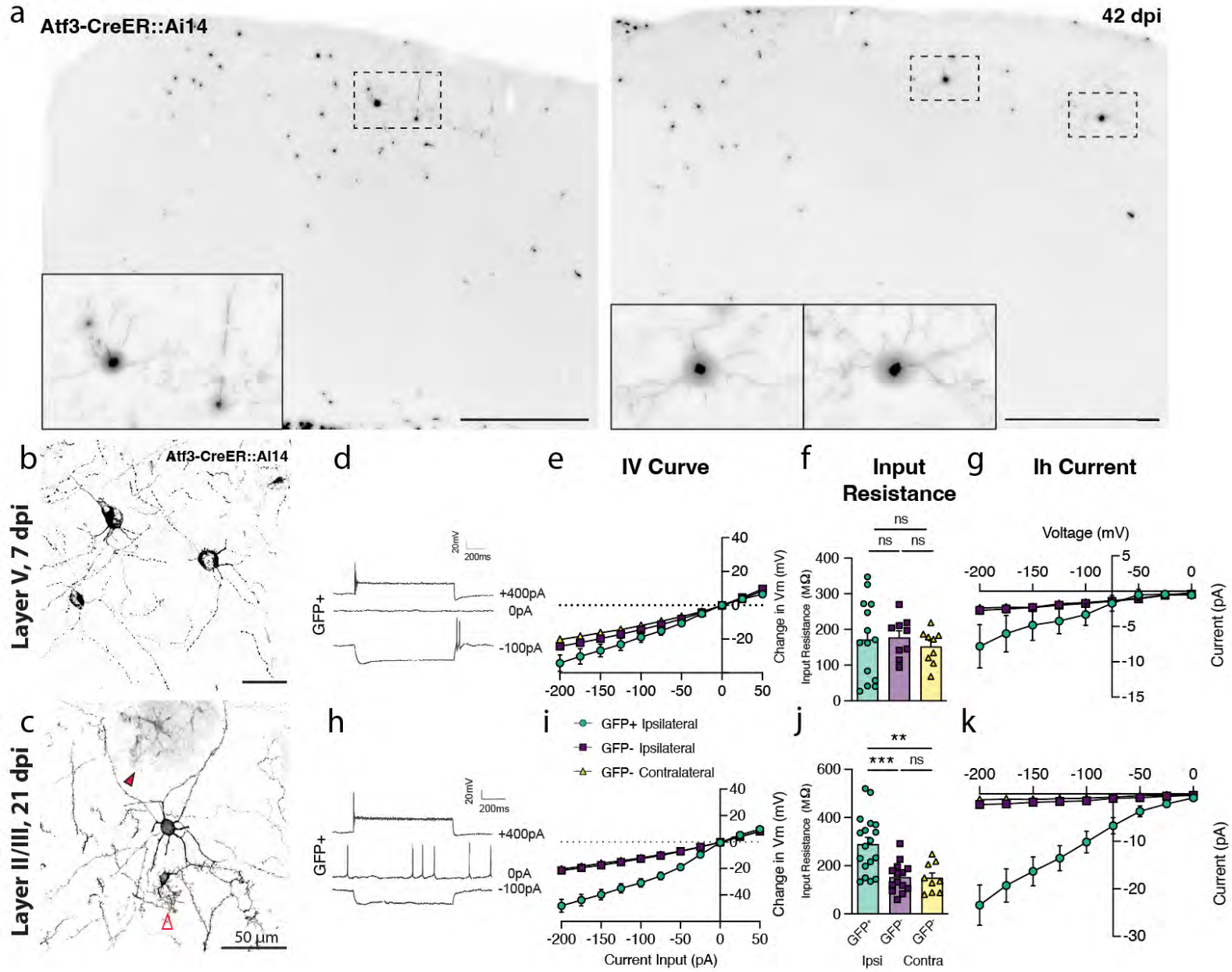

Supplemental Figure 7. Layer II/III Atf3-expressing neuron survival and electrophysiological properties. a. Low magnification images of the ipsilateral cortex of Atf3-CreER::Ai14 mTBI mice at 42 dpi showing surviving neurons and glia. Insets highlight examples of surviving layer II/III neurons. **b.** High magnification image highlighting degeneration of layer V Atf3-CreER::Ai14 neurons at 7 dpi. **c.** High magnification image highlighting an intact layer II/III Atf3-CreER::Ai14 neuron at 21 dpi. Image includes a Atf3-Ai14 microglion (bottom, open arrowhead) and astrocyte (top, closed arrowhead). **d.** Additional example traces of a layer V neuron at 7 dpi. Quantifications of **e.** IV curve, **f.** input resistance, **g.** Ih current in 7 dpi layer V neurons. **h.** Additional example traces of a layer II/III neuron at 21 dpi showing tonic firing. Quantifications of **i.** IV curve **j.** input resistance **k.** Ih current in 21 dpi layer II/III neurons. For IV curve and Ih current graphs, points represent the average of all neurons per group, error bars represent SEM. For input resistance, each point represents one neuron recorded from N = 2-3 animals. Low magnification scale bars, 500 μm. High magnification scale bars, 50 μm.

Supplemental Figure 8

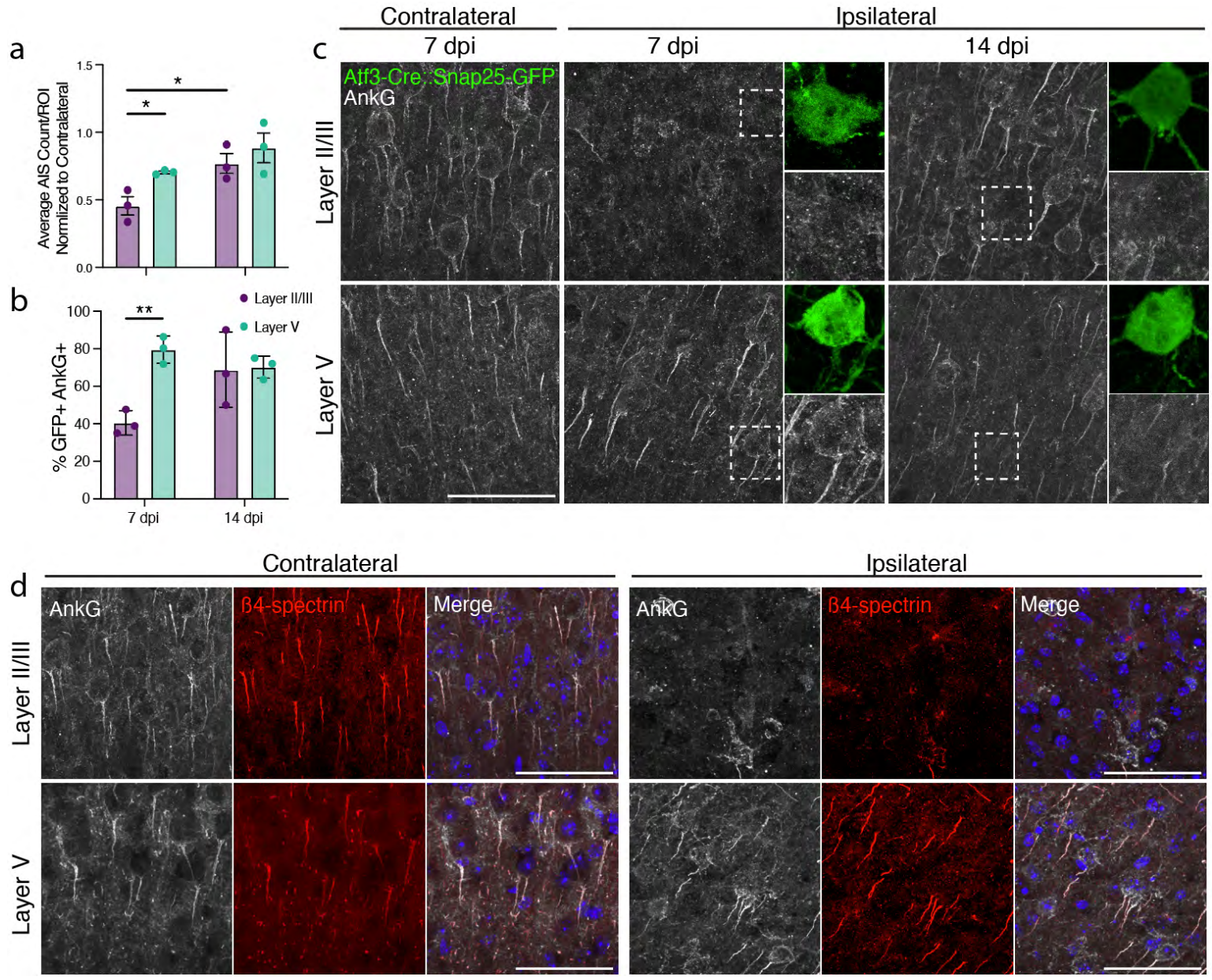

Supplemental Figure 8. Axon initial segments are transiently lost in layer II/III neurons following mTBI. **a.** Quantification of average number of AnkG+ axon initial segments in layer V and layer II/III at 7 dpi and 14 dpi showing a relative reduction in layer II/III at 7 dpi. **b.** Quantification of percent of GFP+ neurons in Atf3-GFP mice with an AnkG+ axon initial segment in layer V and layer II/III at 7dpi and 14 dpi showing a transient loss of axon initial segments in layer II/III neurons. **c.** Example 63X images of AnkG+ axon initial segments in the contralateral cortex at 7 dpi and in the ipsilateral cortex at 7 and 14 dpi in layer II/III and layer V. Insets highlight GFP+ neurons and their axon initial segments. **d.** Example high magnification images of AnkG and β4-spectrin in layer V and layer II/III in the contralateral and ipsilateral cortex at 7 dpi confirming loss of the axon initial segment and not AnkG immunoreactivity. Merge includes DAPI expression. For **a** and **b**, each point represents the average of 3-4 ROIs per 3-4 sections per animal. * $P < 0.05$, ** $P < 0.005$, by unpaired t-test. Scale bars, 50 µm.

Supplemental Figure 9

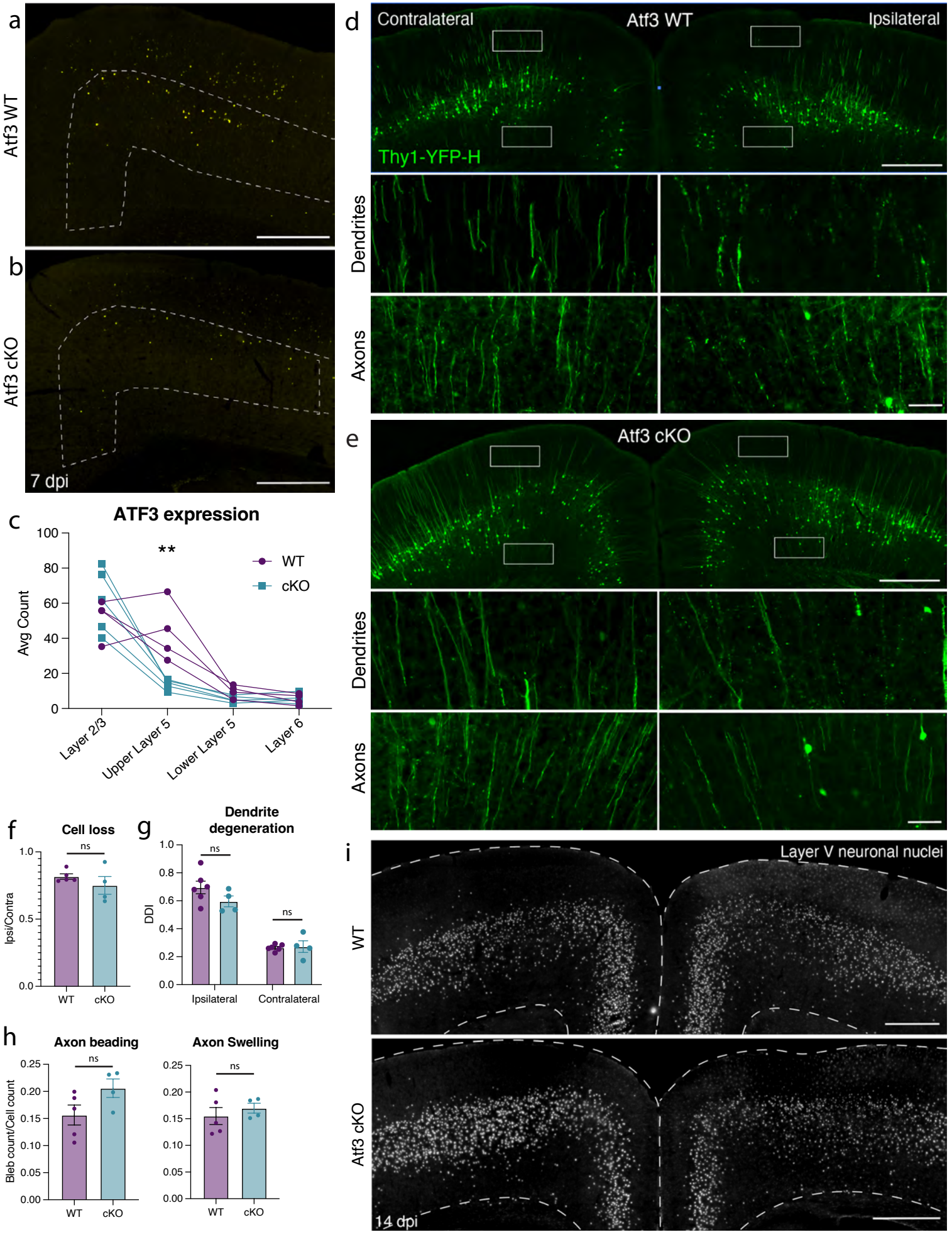

Supplemental Figure 9. Deletion of Atf3 in layer V neurons is not sufficient to prevent neuron degeneration. a. ATF3 expression in ipsilateral cortex at 7 dpi in a wildtype (WT) mouse. Layer V is outlined. **b.** ATF3 expression in the ipsilateral cortex of an Atf3 cKO mouse highlighting a reduction of Atf3 in layer V (outlined). Remaining cells are likely neurons outside of the Rbp4-Cre lineage or ATF3-expressing glia. **c.** Quantification of ATF3 protein expression by cortical layer validating layer V-specific knockout in Atf3 cKO animals. Remaining expression is likely non-neuronal. Each point represents one animal and the average of 3-4 sections. **d.** Thy1-YFP expression in a WT animal with insets highlighting dendrites and axons in the ipsilateral and contralateral cortices. **e.** Thy1-YFP expression in an Atf3 cKO animal with insets highlighting dendrites and axons on the ipsilateral and contralateral cortices. **f.** Quantification of nuclei in the ipsilateral cortex normalized to contralateral cortex at 14 dpi based on such images as in i showing no change in Atf3 cKO. **g.** Dendrite degeneration quantifications from Thy1-YFP animals (examples shown in d,e) revealing no change in Atf3 cKO. **h.** Axon beading and swelling quantifications from Thy1-YFP animals (examples shown in d,e) revealing no change in Atf3 cKO. **I.** Cre-dependent labeling of nuclei in WT and Atf3 cKO animals at 14 dpi. ** $P < 0.005$, by unpaired t-test. ns: not significant. Scale bars, 500 µm.

Supplemental Figure 10

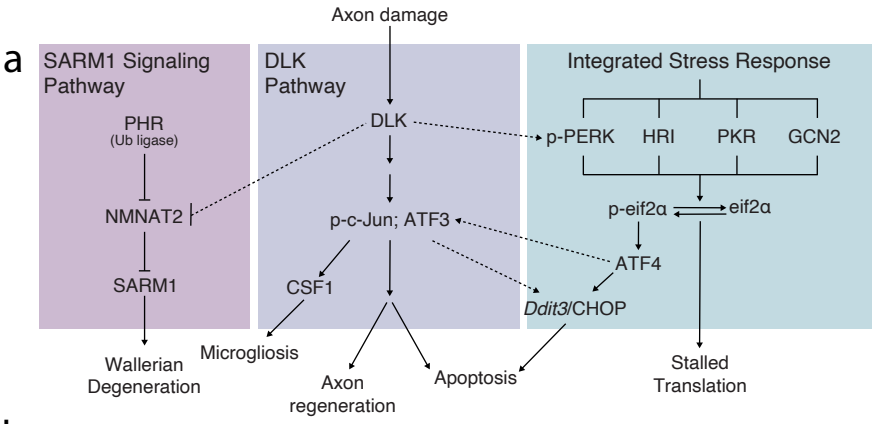

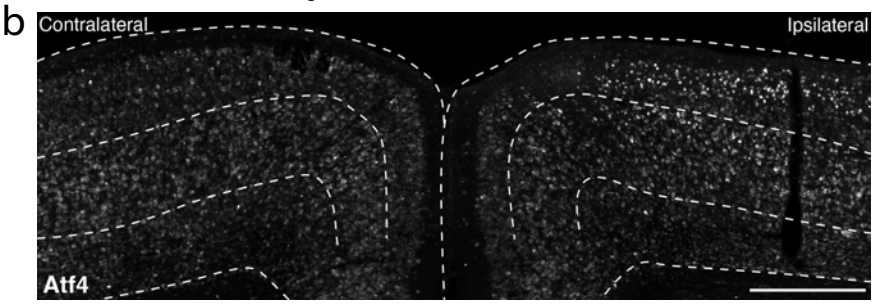

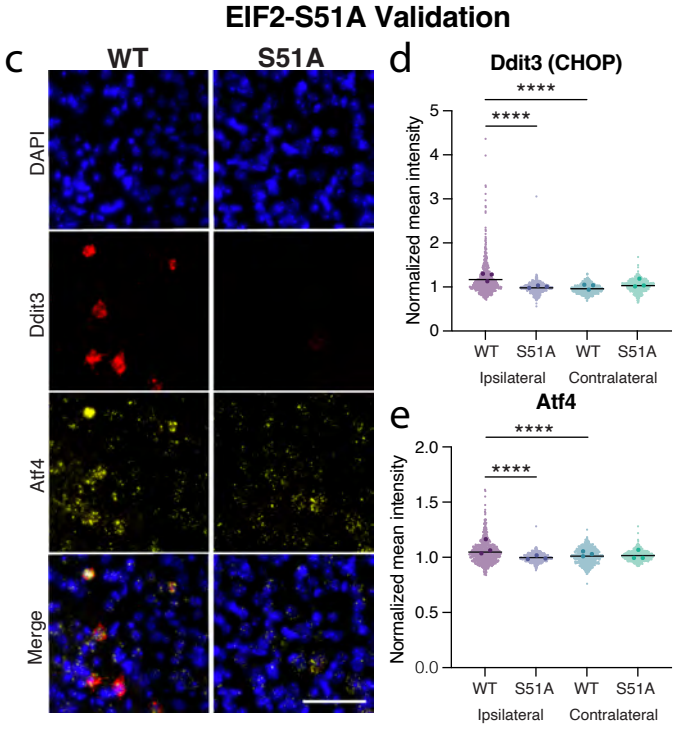

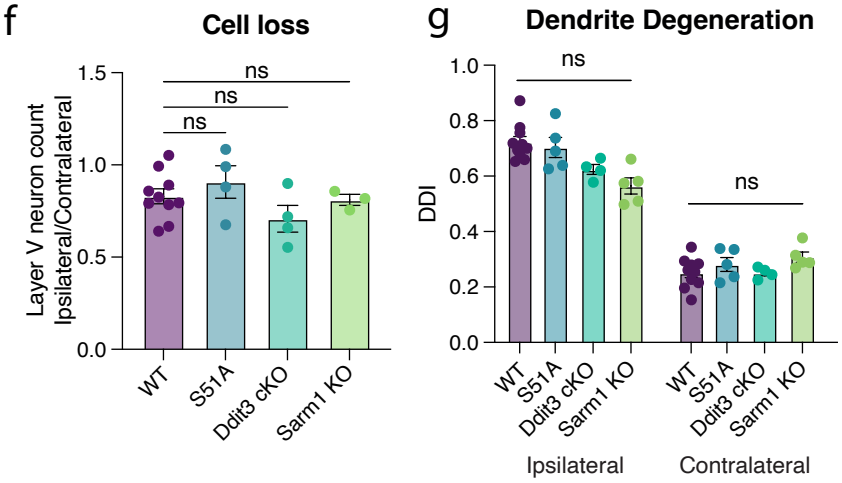

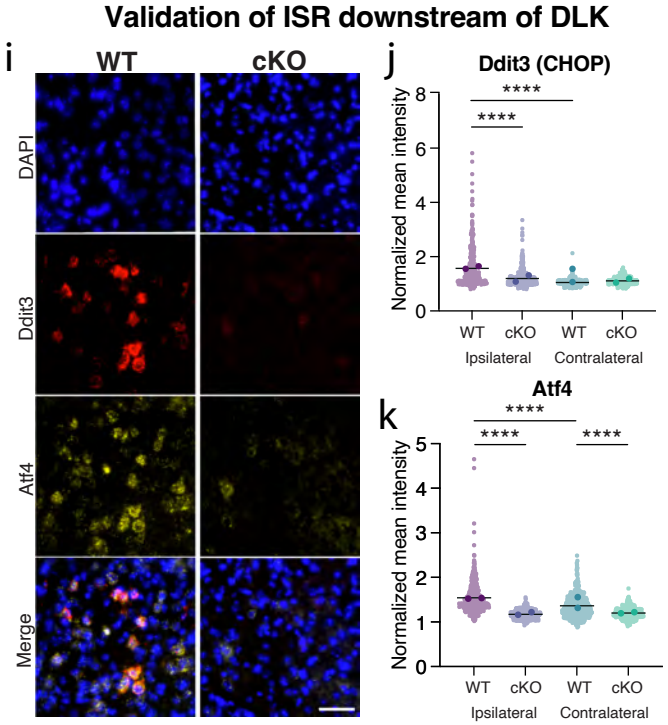

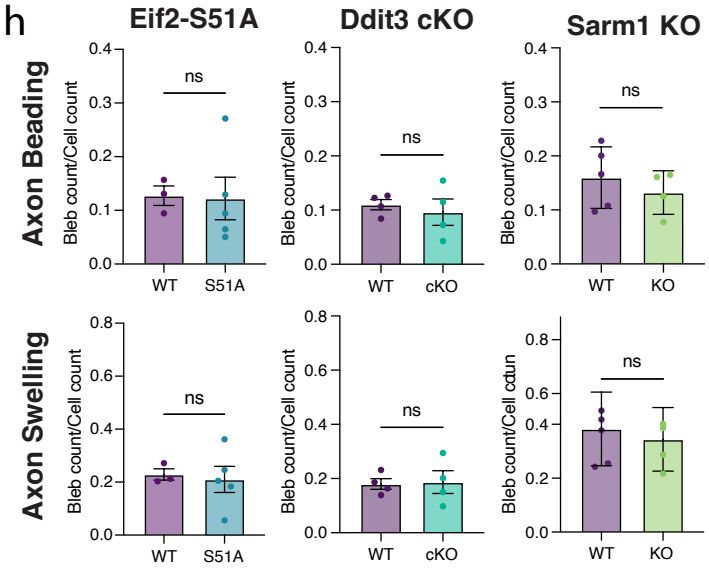

Supplemental Figure 10. Stress response pathways downstream of DLK are not sufficient to induce layer V neuron death. a. A diagram summarizing the interactions between the DLK, SARM1, and integrated stress response pathways and their major effectors. **b.** *In situ* hybridization of *Atf4*, the major effector of the integrated stress response, in the WT mTBI cortex at 7 dpi showing increased mRNA expression in ipsilateral layer V and layer II/III. Layer V is outlined. **c.** Validation of ISR knockdown in the EIF2-S51A mouse, showing *in situ* hybridization of *Atf4* and *Ddit3* in ipsilateral layer V of WT and S51A mice. **d.** Quantification of *Ddit3* (protein name CHOP) *in situ* hybridization in ipsilateral and contralateral layer V of WT and S51A animals. **e.** Quantification of *Atf4 in situ* hybridization in ipsilateral and contralateral layer V of WT and S51A animals. **f.** Quantification of cell loss in layer V of all knockout lines at 14 dpi measured as the ratio of ipsilateral to contralateral cell count, showing that cell loss is insignificantly improved by each manipulation. For all cKO mice, Cre-dependent Sun1-GFP was counted. For KO animals, Thy1-YFP cell bodies were counted. N= 5 WT Thy1-YFP and N= 5 WT cKO were pooled in the WT condition. **g.** Quantification of dendrite degeneration in all knockout lines at 7 dpi showing insignificant changes compared to wildtype. **h.** Quantification of axon pathology in the ipsilateral cortex of all knockout lines, measured as axon beading (fragments with area < 10 µm2) or axon swellings (fragments with area > 10 µm2), showing insignificant changes compared to wildtype. All knockouts are compared to littermate controls. **i.** Validation that the ISR is downstream of Dlk showing *in situ* hybridization of *Atf4* and *Ddit3* in ipsilateral layer V of Dlk WT and Dlk cKO mice. **j.** Quantification of *Ddit3* (protein name CHOP) *in situ* hybridization in ipsilateral and contralateral layer V of Dlk WT and Dlk cKO animals. **k.** Quantification of *Atf4 in situ* hybridization in ipsilateral and contralateral layer V of Dlk WT and Dlk cKO animals. For **d**, **e**, **j**, **k**, Average per animal and value per cell are displayed. For **f-h,** each point represents the average of 3-4 sections per animal. **** $P < 0.0001$, Tukey's multiple comparisons test, based on measure of each cell. ns: not significant based on unpaired t-test compared to WT. Low magnification scale bars, 500 µm. High magnification scale bar, 50 µm.

Supplemental Figure 11

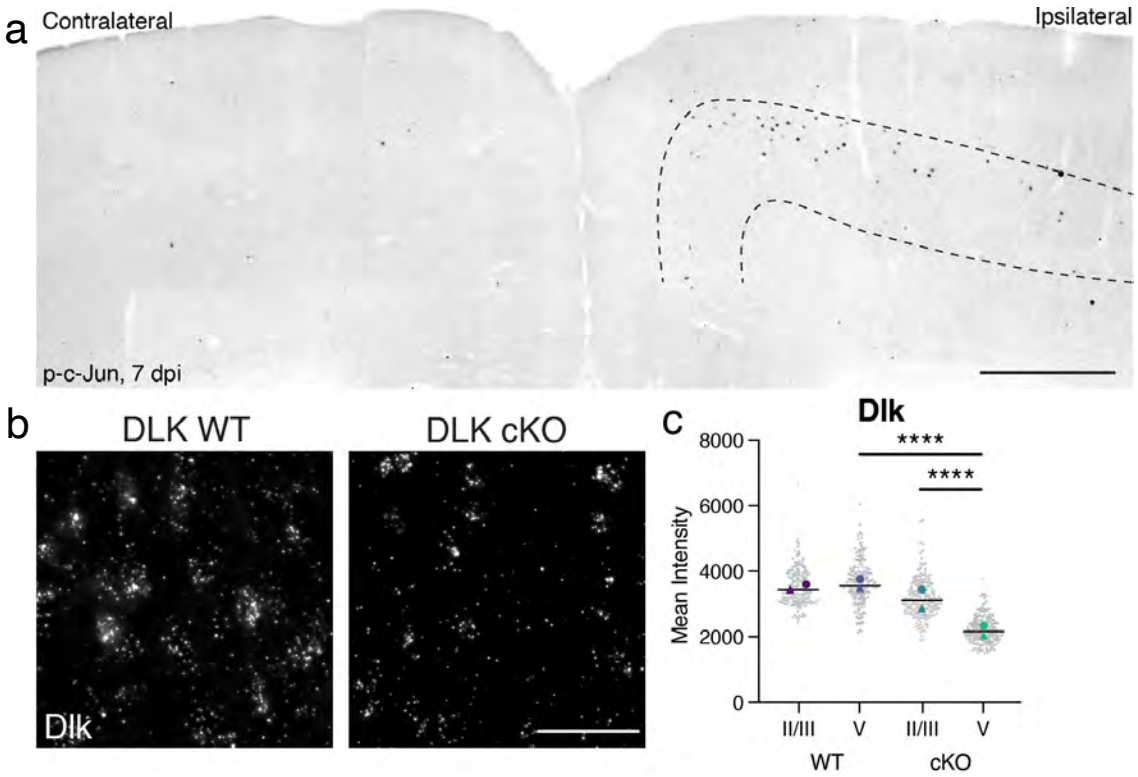

Supplemental Figure 11. Dlk cKO leads to a reduction in layer V Dlk mRNA and is neuroprotective. a. Low magnification image of p-c-Jun in the ipsilateral and contralateral cortices of a WT mouse at 7 dpi showing higher expression in ipsilateral layer V (outlined) and no expression in the contralateral cortex. **b.** High magnification images of ISH for full-length Dlk mRNA in layer V in WT and cKO animals showing a reduction in Dlk cKO. The full length probe still detects mRNA sequence in the cKO animals, with lower intensity signal reflecting cKO. **c.** Quantification of mean intensity of Dlk mRNA in layer II/III and layer V of WT and cKO animals showing a layer V-specific reduction in cKO animals. Average per animal and value per cell are displayed. Each shape represents one animal. Quantifications from N=2 animals and 2 sections per animal. **d.** Thy1-YFP expression in a WT animal with insets highlighting dendrites and axons on the ipsilateral and contralateral cortices. **e.** Thy1-YFP expression in a Dlk cKO animal with insets highlighting dendrites and axons on the ipsilateral and contralateral cortices. **** $P < 0.0001$, Tukey's multiple comparisons test, based on measure of each cell. Low magnification scale bar, 500 µm. High magnification scale bar, 50 µm.

Supplemental Figure 12

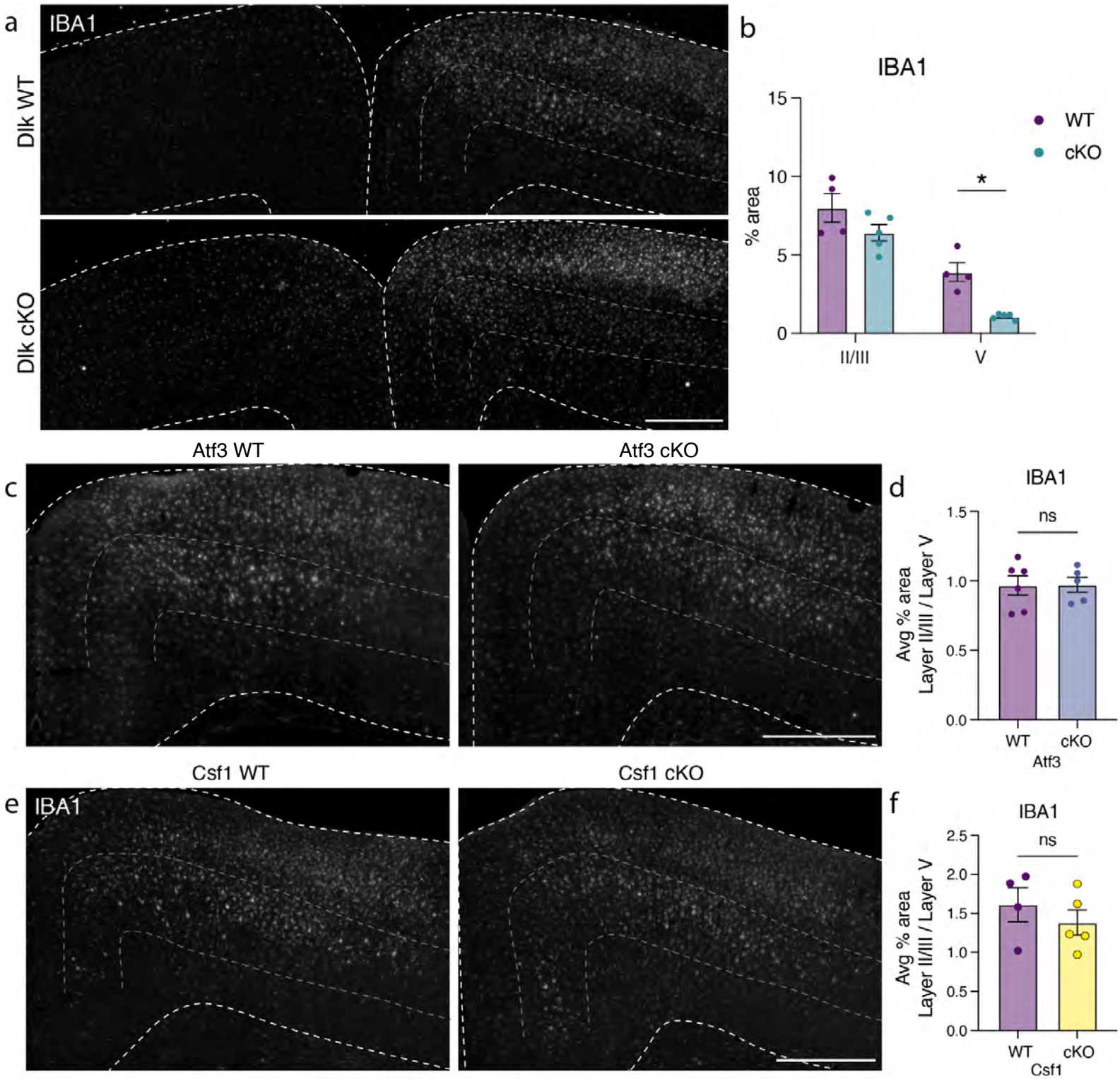

Supplemental Figure 12. DLK deletion leads to a decrease in cortical microgliosis in a Csf1- and Atf3-independent manner. a. IBA1 immunostaining in a DLK WT and Dlk cKO cortex showing that microgliosis is reduced in layer V, where DLK is deleted. Layer V is outlined. **b.** Quantification of percent area of IBA1 immunostaining in layer II/III compared to layer V in WT and cKO animals. **c.** Immunostaining of IBA1 in the ipsilateral cortex of Atf3 WT and cKO animals at 7 dpi showing no effect on microgliosis. Laye r V is outlined. **d.** Quantification of IBA1 percent area in Atf3 WT and cKO cortices, shown as layer II/III percent area over layer V percent area. **e.** Immunostaining of IBA1 in the ipsilateral cortex of Csf1 WT and cKO animals at 7 dpi showing that cortical microgliosis after mTBI is not Csf1-dependent. Layer V is outlined. **f.** Quantification of IBA1 percent area in Csf1 WT and cKO cortices, shown as layer II/III percent area over layer V percent area. * $P < 0.05$, by unpaired t-test. ns: not significant. Scale bars, 500 µm.